Geochemistry 85 (2025) 126326

Contents lists available at ScienceDirect

Geochemistry

journal homepage: www.elsevier.com/locate/chemer

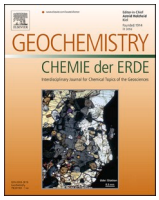

Mineralogical, fluid inclusion, and stable isotope constraints on the genesis of Keban Pb—Zn skarn deposit, southeast Anatolia

Ece Kırat [a,b,*], Halim Mutlu [c]

[a] School of Earth and Environmental Sciences, Cardiff University, CF10 3AT Cardiff, UK
[b] General Directorate of Mineral Research and Exploration, Ankara, Turkey
[c] Department of Geological Engineering, Ankara University, Gölbaşı, Ankara, Turkey

ARTICLE INFO

Handling Editor: Astrid Holzheid

Keywords:
Keban skarn deposit
Mineral chemistry
Fluid inclusion
C-O-S isotopes
Crystallization conditions

ABSTRACT

The Keban Pb—Zn deposit is located in the Elazığ district, southeastern Turkey and hosted by the Permo-Triassic/Permo-Carboniferous Keban Metamorphics and the Late Cretaceous-Paleocene Keban Magmatics. Mineralization develops as disseminated, veins and massive types of ore within alkali syenite porphyry, sericite-chlorite banded calc-schist and dolomitic limestone.

Three paragenetic stages of skarn formation and ore deposition are recognized in the Keban Pb—Zn deposit: prograde (stage I), retrograde-sulfide (stage II), and supergene (stage III). The endoskarn forming a narrow zone is composed of grossular (Grt 1), Fe-rich grossular (Grt 2) and andradite (Grt 3) with diopside and plagioclase. The exoskarn comprises grossular (Grt 4), pyroxene and vesuvianite. Ore minerals include galena, sphalerite, chalcopyrite, magnetite, hematite, molybdenite, and pyrite accompanied in small quantities by pyrrhotite, arsenopyrite, manganese oxides, native gold, and sulfosalts. Mineral chemistry of garnets suggests that Grt 1 precipitated under a low water/rock (W/R) ratio and relatively reduced conditions. Grt 2 with strong oscillatory zoning and Grt 3 with high Fe^{3+} contents were formed under infiltration metasomatism with high W/R ratios. When the water–rock intereaction was decreased, Grt 4 and vesuvianite were affected by Al-bearing residual metasomatic fluids that are derived from calc-schist under reduced conditions.

Depletion of $\delta^{13}C$ and $\delta^{18}O$ in skarn calcites is largely controlled by hydrothermal fluid infiltration and meteoric water influx. Microthermometric measurements support that magmatic fluids comprising the stage I (473 to 572 °C; 11.9 wt% NaCl eq.) were sequentially mixed with meteoric waters of stage II (230 to 524 °C; 0.8.-6.6 wt% NaCl eq). Based on FI trapping pressures and depths of the boiling system, the mineralization developed after boiling during the retrograde stage in a shallow environment characterized by low to moderate temperatures and low salinities, within the pressure and depth range of ~100–500 bar and < 1.5 km, respectively. $\delta^{34}S$ values of sulfide minerals are between −8.5 and + 2.1 ‰ indicating that ore-forming fluids and metals originated principally from a magmatic-hydrothermal source. High Fe, Mn and Ga contents of sphalerites might point to deposition at low to moderate temperature conditions and trace element concentrations imply that mineralization took place at distal part of the skarn system.

1. Introduction

Skarn deposits occur in a wide range of host rocks with a variable geologic age (Precambrian to Late Tertiary), tectonic setting, and ore metal type (Einaudi and Burt, 1982). The variety of factors that control the formation of skarn systems is not limited to this but also includes the origin, temperature, and salinity of the ore-forming fluids (Meinert et al., 2005). Most of the economical skarn deposits are relatively young (e.g. Tertiary), since skarnization is presumably a near-surface process and the erosion might have removed the older deposits (e.g., Burt, 1977; Misra, 2000), and the magmatic-hydrothermal processes associated with dioritic-granitic magmatism in orogenic belts exert a great control over their formation. As a part of the Alpine-Himalayan orogenic belt, Turkey experienced several geodynamic processes including subduction of the Tethys oceanic lithosphere, continental collision, and post-collisional magmatism. The consumption of Paleo- and Neo-Tethys oceans by a northward subduction beneath the Eurasian plate resulted in the emplacement of an ophiolitic mélange that formed the crust presently

* Corresponding author at: School of Earth and Environmental Sciences, Cardiff University, CF10 3AT Cardiff, UK.
E-mail address: kirate@cardiff.ac.uk (E. Kırat).

https://doi.org/10.1016/j.chemer.2025.126326
Received 15 May 2025; Received in revised form 18 August 2025; Accepted 18 August 2025
Available online 22 August 2025
0009-2819/© 2025 The Authors. Published by Elsevier GmbH. This is an open access article under the CC BY license (http://creativecommons.org/licenses/by/4.0/).

exposed over extensive areas in Anatolia (Şengör and Yılmaz, 1981). The decrease in the rate of convergence and subsequent post-collisional extensional tectonics gave rise to the existence of several magmatic episodes (Fig. 1a) (Savostin et al., 1986; Kaymakçı et al., 2006).

The spatio-temporal distribution of plutonism within the southeastern Anatolian orogenic belt shows several groups: (1) Late Cretaceous and Eocene rocks exposing around Baskil, Göksun, Malatya and Keban (Parlak, 2006; Robertson et al., 2007; Rızaoğlu et al., 2009; Kürüm et al., 2008; İmer et al., 2013; Kuşcu et al., 2019; Nurlu et al., 2022; Ersoy et al., 2024); (2) Late Oligocene magmatics in Cevizlidere of the Tunceli Province (e.g., İmer et al., 2015); (3) magmatics rocks of early Miocene and onwards (Pearce et al., 1990). There is a consensus that Late Cretaceous to Eocene magmatism in this part of Anatolia is of subduction-related arc/back-arc type (Parlak, 2006; Parlak et al., 2004; İmer et al., 2013; Nurlu et al., 2022; Ersoy et al., 2024). The Oligocene magmatism is likely *syn*-collisional however early Miocene and onwards are represented by post-collisional magmatics. Only Kuşcu et al. (2010, 2019) consider the Cretaceous-Eocene magmatism as post-collisional.

Porphyry and skarn systems distributed in the central Turkey and southeastern Anatolian orogenic belt are mostly hosted in the A-type granitoids (Boztuğ et al., 2007; Liu et al., 2022; Ertürk et al., 2022; Ersoy et al., 2024). Keban district intrusions are especially alkaline-shoshonitic in chemistry. The only typical I-type magmatics in this region are Late Cretaceous Baskil and Eocene Çaltı, Çöpler, and Kabataş intrusions (Kuşcu et al., 2013; İmer et al., 2013). Skarn deposits associated with the Late Cretaceous alkaline magmatism are generally typical of eastern Turkey. The majority of the deposits in this region comprise Fe, Pb—Zn, and Cu-Mo-W-F type mineralizations which include Divriği (Kuşcu et al., 2002), Dumluca, Hasançelebi IOCG systems (Kuşcu et al., 2011), Çöpler (İliç) porphyry-epithermal Cu—Au system (İmer et al., 2016), Bızmişen-Çaltı (İliç), Aşvan-Birvan (Keban) and Dedeyazı-Çavuşlu (Doğanşehir) Fe skarns; Keban Fe- and Pb—Zn skarn; and Keban Cu-Mo-W-F skarn deposits (Yıldırım et al., 2019b) (Fig. 1b).

The skarn deposit in the Keban district, the southeastern Anatolia, occurs at the contact between Late Cretaceous alkali syenite porphyry and Permo-Triassic carbonaceous meta-clastic rocks. The resulting contact metasomatism has led to the formation of a Cu-Mo-W-F-type mineralization. The most prominent skarn mineralizations in the Keban area comprise the Derebaca–Fırat Main Pit (Pb—Zn), Zeytindağ–Haznemağara–Sulumağara–Molaveli Ridges (Pb—Zn), Zeryan Dere (Pb-Zn-Fe) and Asker Hill–Nallıziyaret–Keban Dere deposits (Cu-Mo-W) in the Doğu Fırat and Şeyhlik Dere (Pb—Zn) and Karamağara Dere deposits (Cu-Mo-F-Pb-Zn) along the Batı Fırat (Fig. 1c).

Mining in the polymetallic Keban province dates back to the Hittite period (~2000 BCE) (Seeliger et al., 1985; Yıldırım et al., 2019a). During exploration studies in the 1980s, Etibank, the previous license holder of the mine, discovered nearly 10 million tons of reserve with average grades of 1 % Cu, 2 % Pb, and 50 g/t Ag (Hanelçi, 1991; Yıldırım et al., 2019b). An intense drilling programme conducted in the last

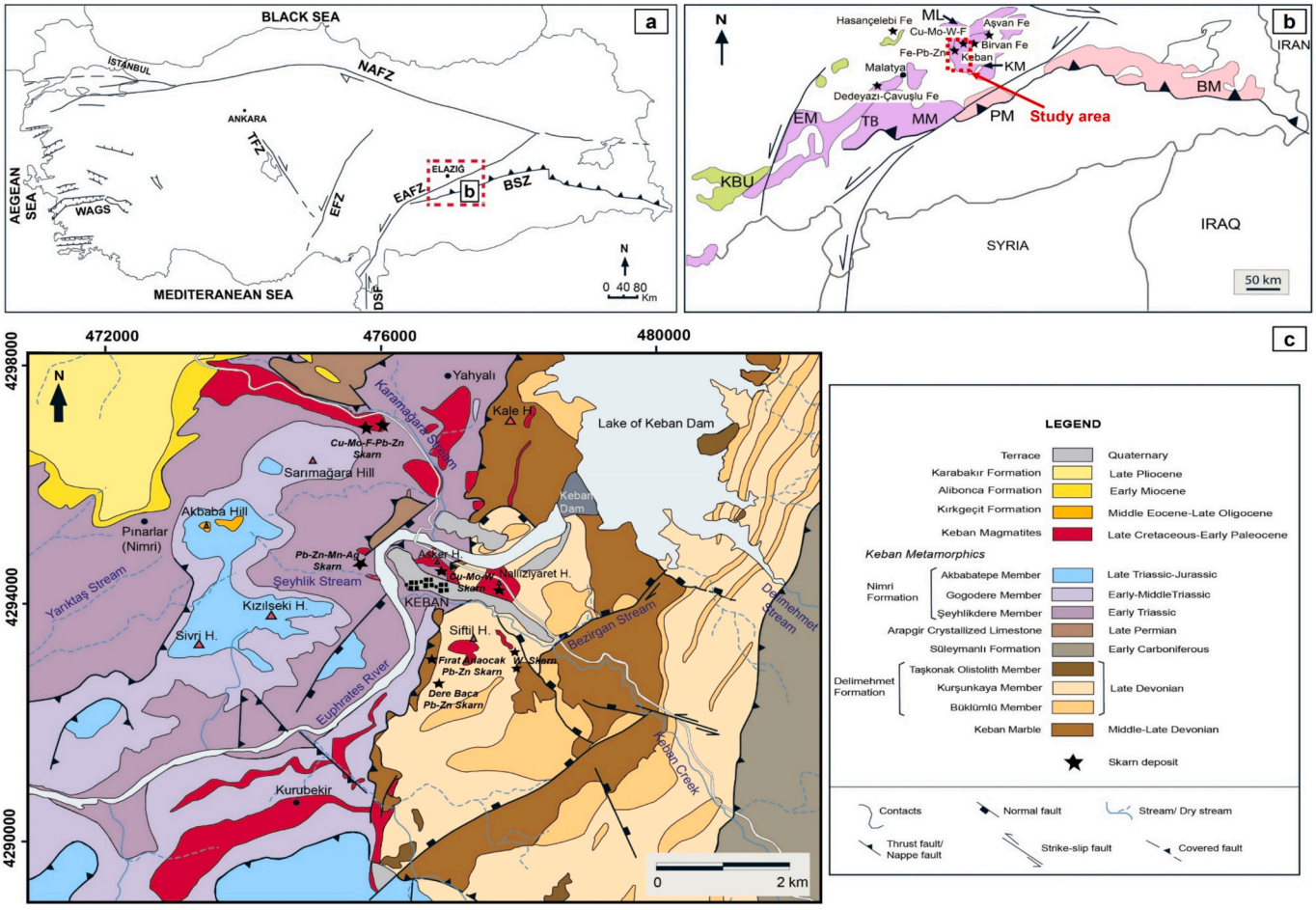

Fig. 1. a. Location of the study area with the tectonic subdivisions of Anatolia and adjacent regions (BSZ: Bitlis Suture Zone, NAFZ: North Anatolian Fault Zone, EAFZ: East Anatolian Fault Zone and WAGS: Western Anatolian Graben System, EFZ: Ecemiş Fault Zone), b. Simplified geological map of the Eastern Tauride orogenic belt illustrating the main metamorphites and skarn ore deposits (TB: Tauride Belt including EM: Engizek metamorphites, MM: Malatya metamorphites, KM: Keban metamorphites and ML: Munzur limestones; BM: Bitlis Metamorphites; PM: Pütürge metamorphites; KBU: Kütahya-Bolkardağı Union) (Modified Özgül, 1976; Moix et al., 2007; Göncüoğlu, 2011; Kaya, 2016) c. Geological map of the Elazığ-Keban district (Modified from Kaya, 2016).

decade by the General Directorate of Mineral Research and Exploration (MTA) (Fig. 2a) substantially increased the average ore grades at Keban (e.g., 4.5 % Pb, 5.3 % Zn) which hosts nearly 86,800 tons of proven, 48,000 tons of probable and one million tons of possible reserves (Kuşcu, 2019).

A number of studies were conducted that discuss the geology, mineralogy, geochemistry, petrography, and the origin of mineralization in the region (Hanelçi, 1989, 1991; Yılmaz et al., 1992; Çelebi, 1997; Çelebi and Hanelçi, 1998; Çalık and Öngen, 2000; Kalendar and Hanelçi, 2004; Yiğit, 2009; Kalender, 2011; Kürüm, 2013; Kuşcu, 2019; Kuşcu et al., 2013; Yıldırım et al., 2019a, 2019b). Although the skarn zone and the host alkali syenite porphyry at Keban have been the focus of several mineralogical and petrographic research (e.g., Çalık and Öngen, 2000; Kalender, 2011; Kürüm, 2013; Yıldırım et al., 2019a, 2019b), limited data are available for geochemical and isotopic controls on mineralization and skarn formation processes. Therefore, in this study, the mineral paragenesis, the P-T conditions, composition, and evolution of the ore-forming fluids that govern the economic potential of

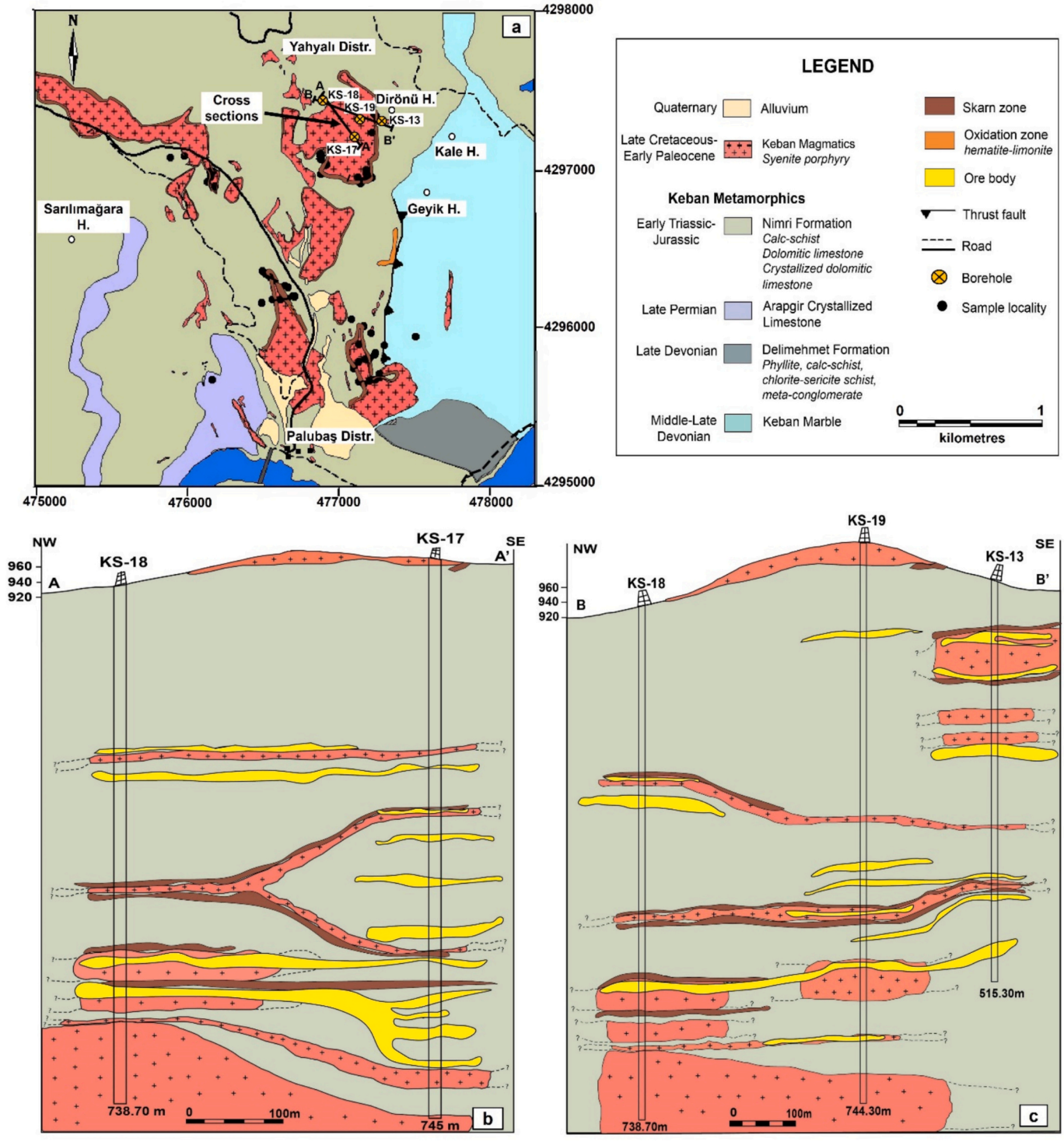

Fig. 2. a. Geological map of the Keban district and subsurface distribution of alteration zones (modified from Balçık et al., 1978 and Yıldırım et al., 2019a, 2019b, locations of drill hole from Yıldırım et al., 2019a), b-c. Cross-sections of the Keban-West Euphrates.

Keban Pb—Zn mineralization are examined using a variety of chemical and mineralogical analyses which include ore petrography, mineral chemistry of skarn minerals, fluid inclusions, C—O isotope of calcites, and S isotope of sulfides. For this purpose, the following studies were carried out: (1) detailed mineralogical and petrological descriptions of ore zones; (2) mineral chemistry study to determine mode of formation for each skarn stage; (3) fluid inclusion measurements to explore the origin, nature, evolution, and P–T conditions of hydrothermal fluids; (4) stable isotope analysis of carbonate minerals from the skarn zone and host rock to identify the possible role of volatilization and fluid infiltration in the deposition of skarn minerals; (5) sulfur isotope analysis of sulfides to identify the possible origin of sulfur and ore-forming fluids; and (6) constructing a genetic model of the deposit and comparison our data with various Pb—Zn skarn systems.

2. Regional geology

Tectonic unrest in Turkey is manifested along four major fault zones: Bitlis Suture Zone (BSZ), North Anatolian Fault Zone (NAFZ), East Anatolian Fault Zone (EAFZ) and Western Anatolian Graben System (WAGS). The BSZ was formed by the continent-continent collision of the Eurasian and Arabian plates during the Late Miocene (Fig. 1a) (Şengör and Yılmaz, 1981; Dewey et al., 1986). This suture zone is surrounded at north by the Southeastern Anatolian orogenic belt (SAOB) which is an arcuate mountain chain comprising a variety of magmatic rocks and metamorphites and a range of deposit types including porphyry Cu—Au and Cu—Mo, Pb—Zn, iron oxide and Fe ± Cu skarn (Kuşcu, 2019) and gold hosted in epithermal-style veinlets such as in the Çöpler deposit (Erzincan) (İmer et al., 2013). In the east-west direction, the SAOB comprises the Engizek metamorphics (EM), Malatya metamorphics (MM), Pütürge metamorphics (PM), Keban metamorphics (KM), Munzur limestones (ML) and Bitlis Metamorphites (BM) (Fig. 1b).

The Keban deposit is located in the Eastern Taurus region of the Alpine-Himalayan orogenic belt (Fig. 1a). The Eastern Taurus undergone a substantial crustal deformation, resulting in the formation of Permo-Triassic metamorphic rocks and Late Cretaceous magmatics, which represent the basement rocks in the region. The Keban Metamorphics that are a part of the Alanya Assemblage (Özgül, 1976), comprise platform-type carbonates and clastic rocks that underwent low-grade regional metamorphism.

The Late Cretaceous-Paleocene Keban Magmatics comprising the easternmost branch of the Göksun-Afşin, Doğanşehir, and Baskil granitoids intruded the Keban Metamorphics. Geochemical and isotopic data indicate that Keban Magmatics are metaluminous and alkaline series (e.g. Kürüm, 2013; Yıldırım et al., 2019b). They have A-type affinity and are derived from subduction-modified crustal sources (e.g., Kuşcu et al., 2013; Kürüm, 2013; Akgül, 2015; Yıldırım et al., 2019b; Kırat, 2020). According to Liu et al. (2022) and Ersoy et al. (2024), the alkaline magmatism in eastern Turkey was derived from a shallow asthenospheric mantle source, which had been previously metasomatized by oceanic to continental subduction. They were formed in the late orogenic and within-plate tectonic settings (Kürüm, 2013; Kuşcu et al., 2013). K/Ar dating of micro syenite yielded ages of 76 to 78 Ma (Yazgan, 1984). U—Pb and $^{40}Ar/^{39}Ar$ dating on syenite porphyry indicated ages in the range of 74.8 to 74.1 Ma and 74.08 to 69.9 Ma, respectively (Kuşcu et al., 2013). Alternatively, Liu et al. (2022) highlight a transition from high-K calc-alkaline (Group 1, ~87–77 Ma) to magmatism to Ne-normative alkaline (Group 2 A, ~77–69 Ma) and shoshonitic (Group 2B, ~77–69 Ma) magmatism at ~77 Ma in the eastern Taurid block.

The Keban Magmatics are discordantly overlain by the Eocene Kırkgeçit Formation, which is composed of conglomerate, sandstone, and limestone. Above is the Lower Miocene Alibonca Formation consisting of conglomerate, sandy limestone, and marl. The tuff, olivine basalt, and limestone of the Pliocene Karabakir Formation cover these units with an angular unconformity (Fig. 1c).

3. Local geology

The Permo-Triassic/Permo-Carboniferous Keban Metamorphics consisting of massive crystalline olistoliths, calc-schist, sericite-chlorite schist and crystallized limestones comprise the basement and are served as a significant host lithology for the skarnization. Keban Metamorphics that were intruded by the Late Cretaceous Keban Magmatics include, from oldest to youngest, the Arapgir limestone, Keban Marble, Nimri Formation, and Delimehmet Formation (Fig. 2c). The protolith of the Keban Metamorphics is considered as carbonaceous sandstone (Asutay, 1988).

3.1. Host rocks

The Nimri and Delimehmet Formations are the host rocks of skarn mineralization. Ore-bearing calcic skarn zones with widths of ~5–20 m along contact zones commonly occur within the Early Triassic-Jurasic Nimri Formation in the West Euphrates region (Fig. 2). The Nimri formation, the lowest nappe of the Keban Metamorphics, has been divided into three members: Şeyhlikdere calc-schist member, Gogodere layered dolomitic limestone member and the Akbabatepe dolomitic limestone member (Fig. 1c) (Kaya, 2016). The formation that is widely exposed on both sides of the Euphrates consists of carbonate metaclastic rocks (meta-shale, calc-phyllite, and calc-schist) (Fig. 2a). Carbonate rocks become dominant towards the upper levels (dolomitic limestone) (Kaya, 2016). The calc-shists are generally observed in dirty white, yellowish to gray-green color and cleavages extend parallel to the bedding (Fig. 3a). Meta-pelites (phyllite/calc-phyllite) occur at the base of the calc-schists. They are overlain by crystalline dolomitic limestone consisting of thin meta-pelite interlayers of massive chlorite-sericite phyllites assemblage that occurs in a microgranoblastic texture (Kaya, 2016).

The Keban Marble consisting of white colored, fractured, and massive marble is the oldest unit in the area. It is overlain by the Delimehmet formation of the Late Devonian age. The formation starts with metaconglomerate-metasandstone at the base (Büklümlü Member) and continues with phyllite-chlorite-sericite schist to the top with intrusions of metadiabase dykes (Kurşunkaya Member) and limestone olistoliths (Taşkonak Member). The overlying Early Carboniferous Süleymanlı Member is composed of light-gray or dark, black, organic-rich crystallized limestone-calcschist (Kaya, 2016) (Fig. 1c).

3.2. Plutonic rocks

Keban Magmatics emplaced as a series of sills, stocks and dykes with length varying from a few to several tens of meters (Fig. 2a, 3b, c). They are noticeable with porphyritic texture hosting pinkish-white large K-feldspar phenocrysts in a dark colored groundmass (Fig. 4a, c, i). Alkali syenite and monzo-syenite porphyry are the major plutonic rocks in the region, but the former is more dominant. Alkali syenite porphyry consists of large crystals of idiomorphic and hypidiomorphic nepheline (Fig. 5a) and orthoclase surrounded with fine-grained hypidiomorphic and xenomorphic plagioclase and oligoclase-albite biotite, amphibole, and primary pyroxene, titanite (Fig. 5b), melanite (Ti-andradite), pseudoleucite and cancrinite. Sericitization, argillization, opacitization, and chloritisation are the main alteration types. Alteration of plagioclase leads to alteration of argillization and sericitization (sericite = fine-grained white mica), pyroxene and amphibole are altered to chlorite minerals. Andraditic garnet consisting of subhedral to anhedral brown-red crystals is typically prominent in the contact zone of the intrusives (Fig. 3c, 4e, g). Although the distribution and interrelationships of alterations cannot be determined due to different form of emplacement of the intrusive rocks, the intensity of the alteration in alkaline syenites increases towards calc-silicate units and mineralization. Accessory minerals comprise apatite, zircon, fluorite and opaque minerals such as pyrite, magnetite, and ilmenite. Calcite, sericite, muscovite, and clay minerals are the secondary minerals (e.g., Yıldırım et al., 2019b).

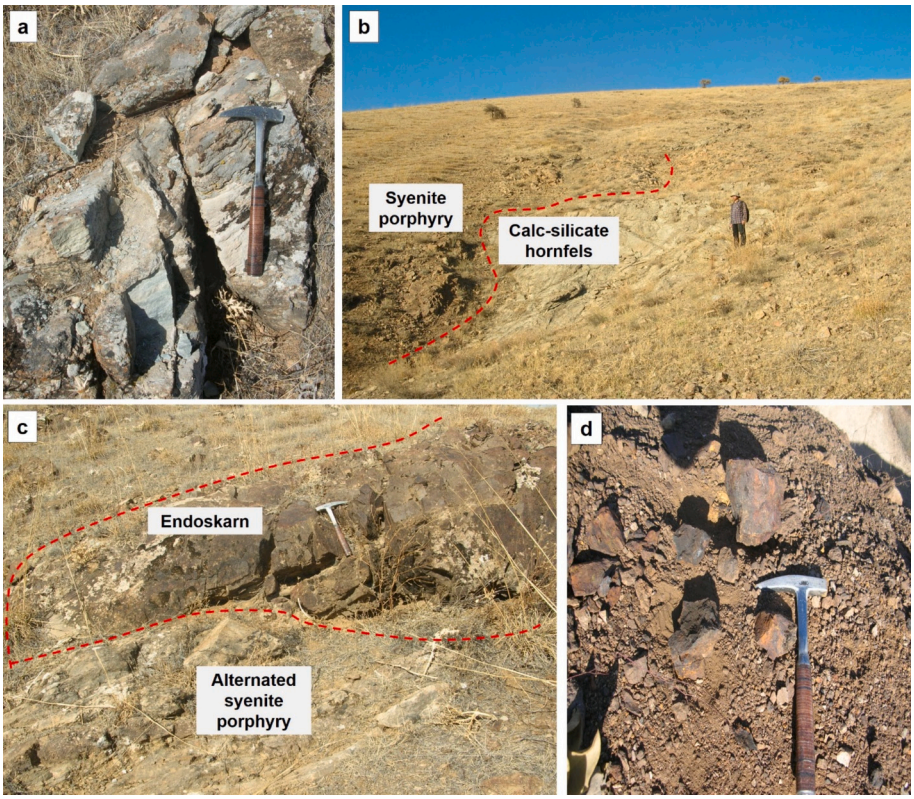

Fig. 3. Field relations of calc-schist, calc-silicate hornfels, alkali syenite porphyry intrusions, and mineralization. a. yellow-green colored calc-schist with cleavage textures, b. the contact zone between syenite porphyry and cal-silicate hornfels, c. the contact between brown-colored endoskarn zone and alternated syenite porphyry, d. sulfur-dominated mineralization from abandoned mine gallery. (For interpretation of the references to color in this figure legend, the reader is referred to the web version of this article.)

4. Contact metamorphism

Calc-silicate hornfels/marble evolved as haloes because of isochemical metamorphism between the intrusive and calcareous metaclastics (Fig. 3b, 4b, c). The degree of metamorphism decreases outward of the igneous intrusions. Hornfels are composed of calcite, quartz, sericite, feldspar, pyroxene, hornblende and garnet. As the degree of recrystallization increases, carbonate rocks with saccharoidal texture show a gradual transition into themarble. As a result of progressive contact metamorphism, pelitic schist, calcareous rocks, and meta-carbonates were converted to hornblende hornfels, pyroxene hornfels, and pyroxene-garnet skarn, respectively (Yıldırım et al., 2019b).

5. Skarn mineralization

The existence of skarnization at the contact zone of the syenitic rocks is the most prominent indicator of a metasomatic process associated with the local injection of magmatic fluids into the wall rock. Extensive magmatism and alteration in the contact zone with the alkali syenite porphyry modified the original N-S trending structures and southward-dipping calcareous rocks. The Permo-Triassic/Permo-Carboniferous Keban Metamorphics, meta-clastic/carbonate rocks and the Late Cretaceous-Paleocene alkali syenite porphyry are the major host rocks of the mineralization. There are several other polymetallic skarn mineralizations in the East Euphrates. The west Euphrates-Keban skarn deposits have been classified into three categories- Cu—Mo skarn (proximal), Pb—Zn skarn (distal) and Au-bearing skarn (Yıldırım et al., 2019b).

The lithology, chemical composition, geometry, and the extent of intrusion affect the size and shape of the skarn zone and the type of mineralization. The Keban skarn zones have widths between 5 and 30 m and range in strike from a few tens of meters to nearly one hundred meters. They have sharp contact with the intrusive body and carbonate rocks (e.g., northeast of Palubaş village) and are irregularly distributed as the intrusive rock displays different forms of emplacement including sills and dykes. The studied skarn zones extending in N-S direction are exposed at the southeast of Yahyalı district, northeast of Palubaş, and southeast and northeast of the Sarılımağara hill (Fig. 1c and 2a). They completely envelop the alkali syenite porphyry (Fig. 2b, c). Skarns of small-scale mineralizations (1 m across) and veinlets (from a few cm to 50–60 cm) within limestone are accompanied by pyrite, sphalerite, galena, and lesser chalcopyrite and native gold (Yıldırım et al., 2019a). Skarnization poorly develops in the alkali syenite porphyry, however, it is quite common at the contact with the carbonate metaclastics without any apparent zoning. The width of skarn is 15–20 m in areas of intrusive rock. The thickness of the endoskarn zone is between a few cm and a few meters in alkali syenite porphyry, which is slightly affected by metasomatism. The exoskarn zone has sharp contacts and propagates towards the metasedimentary rocks. The endoskarn is brown-colored and dominated by garnet, pyroxene, and alkali feldspar (Fig. 3c, 4d, e), whereas the exoskarn is gray-green colored and enriched in garnet, pyroxene, epidote and chlorite (Fig. 4f, g). As a result of metasomatic reactions, prograde zone is overprinted by hydrous minerals such as epidote, chlorite, and sericite (Fig. 4i). The ore-bearing skarn calcites are generally formed within the carbonate metaclastics and along the contacts of the alkali syenite porphyry intrusions (Fig. 4h).

5.1. Skarn mineralogy and paragenesis

Skarn zones in the Keban area form two facies with respect to mineral type/the distance from the contact zone – endo and exoskarn zones. The endoskarn zone occurring in a narrow area (a few cm to one meter)

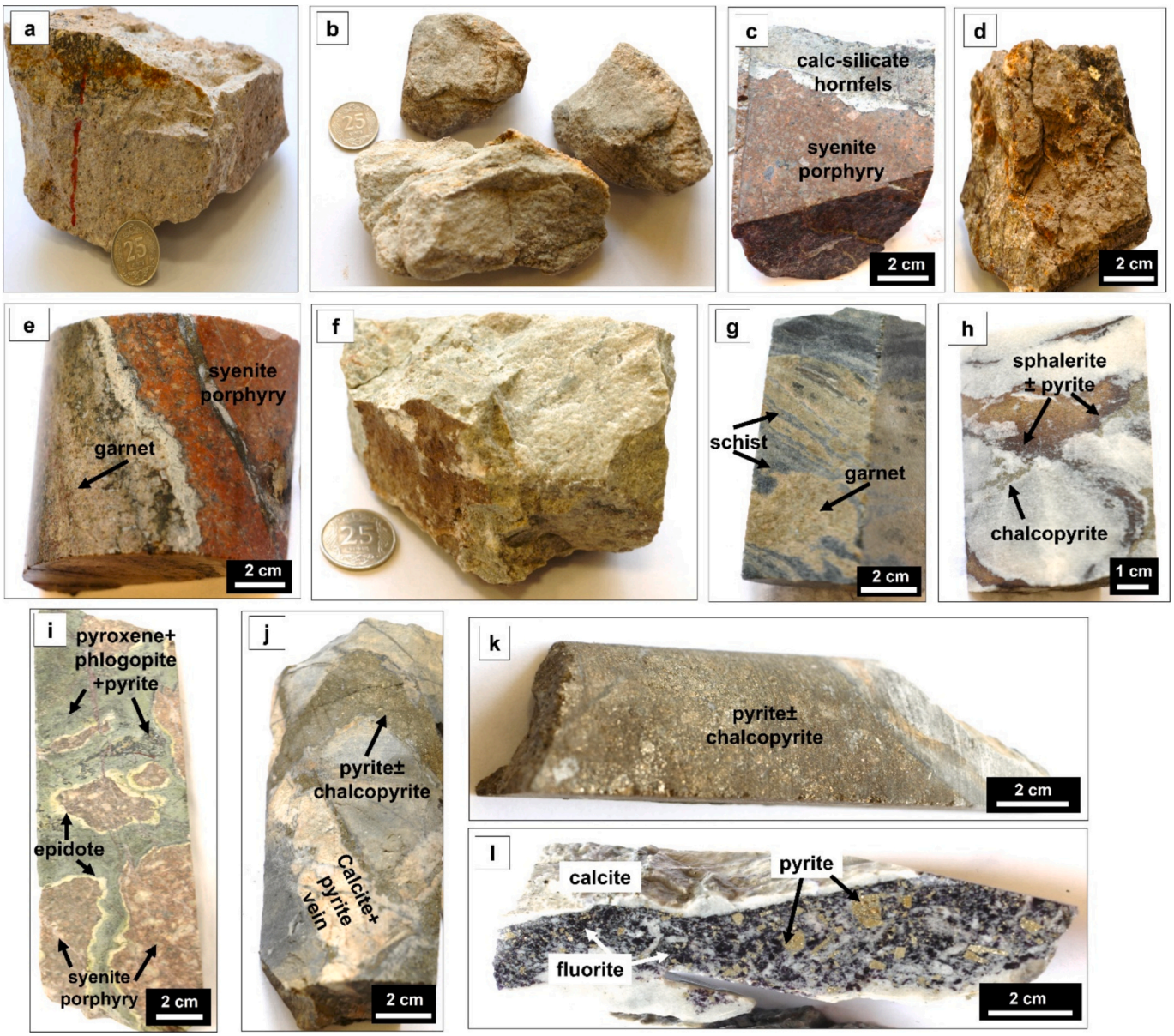

Fig. 4. Hand specimens of intrusive rock, hornfels, skarn zones, and mineralization. a. pinkish-white colored alkali syenite porphyry with large feldspar phenocrysts, b. calc-silicate hornfels with saccharoidal texture, c. calc-silicate hornfels developed around syenite porphyry intrusions, d. garnet and calcite dominated brown-colored endoskarn zone, e. andradite dominated endoskarn zone developed at contact of alkali siyenite porphyry, f. gray-green colored exoskarn zone, g. grossular dominated exoskarn zone in calc-shist, h. skarn calcite with sphalerite, chalcopyrite, and pyrite, i. metasomatic zonations occurred at contact with syenite porphyry, j. massive pyrite± chalcopyrite vein with a thickness of 1.5–2 cm cuts calcite+pyrite vein, k. massive pyrite± chalcopyrite with up to 15 cm of thickness, l. fluorite vein with a thickness of 1–3 cm containing calcite and pyrite crystals. (For interpretation of the references to color in this figure legend, the reader is referred to the web version of this article.)

at the contact or within the intrusive rock is composed of alkali feldspar, plagioclase, calcic pyroxene, and garnet (grossular-andradite) with varying composition and abundance. It appears in brown color as the calcite and andraditic garnet contents are increased. The exoskarn zone contains grossular garnet, calcic pyroxene, and vesuvianite. The zone turns to gray-green in areas where the epidote and chlorite are dominant.

The prograde stage is represented by anhydrous minerals, which include garnet (andradite and grossular), pyroxene (diopside and hedenbergite), vesuvianite and albite. The retrograde phase overprinting the prograde stage corresponds to a temperature decrease and contains several hydrous minerals (e.g., tremolite, actinolite, epidote, biotite, phlogopite, allanite, muscovite, sericite and chlorite), magnetite, hematite and sulfide minerals. Endoskarn and exoskarn are home to both prograde and retrograde stages. The calcic exoskarn that comprises ore minerals was formed under sulfur-rich conditions along with carbonate (rhodochrosite), manganese-rich oxide (primarily pyrolusite) and fluorite. Skarn mineralogy and petrographic characteristics of the Keban deposit are summarized in Table 1. Locations of samples and boreholes KS-17, KS-18, and KS-19 are presented in Supplementary Fig. S1, Supplementary Table T1 and T2.

Mineralization forms within magmatic rocks and commonly in sericite-chlorite banded calc-schist and limestone. It occurs as disseminated, veins and massive types of ore within veins of calcite, quartz, and fluorite. Mineralization is composed of sulfides, oxides and secondary minerals of the supergene zone (Fig. 3d). The ore-bearing calcic exoskarns contain chalcopyrite, pyrite, marcasite, galena, molybdenite, magnetite, and lesser amounts of manganese oxides, arsenopyrite,

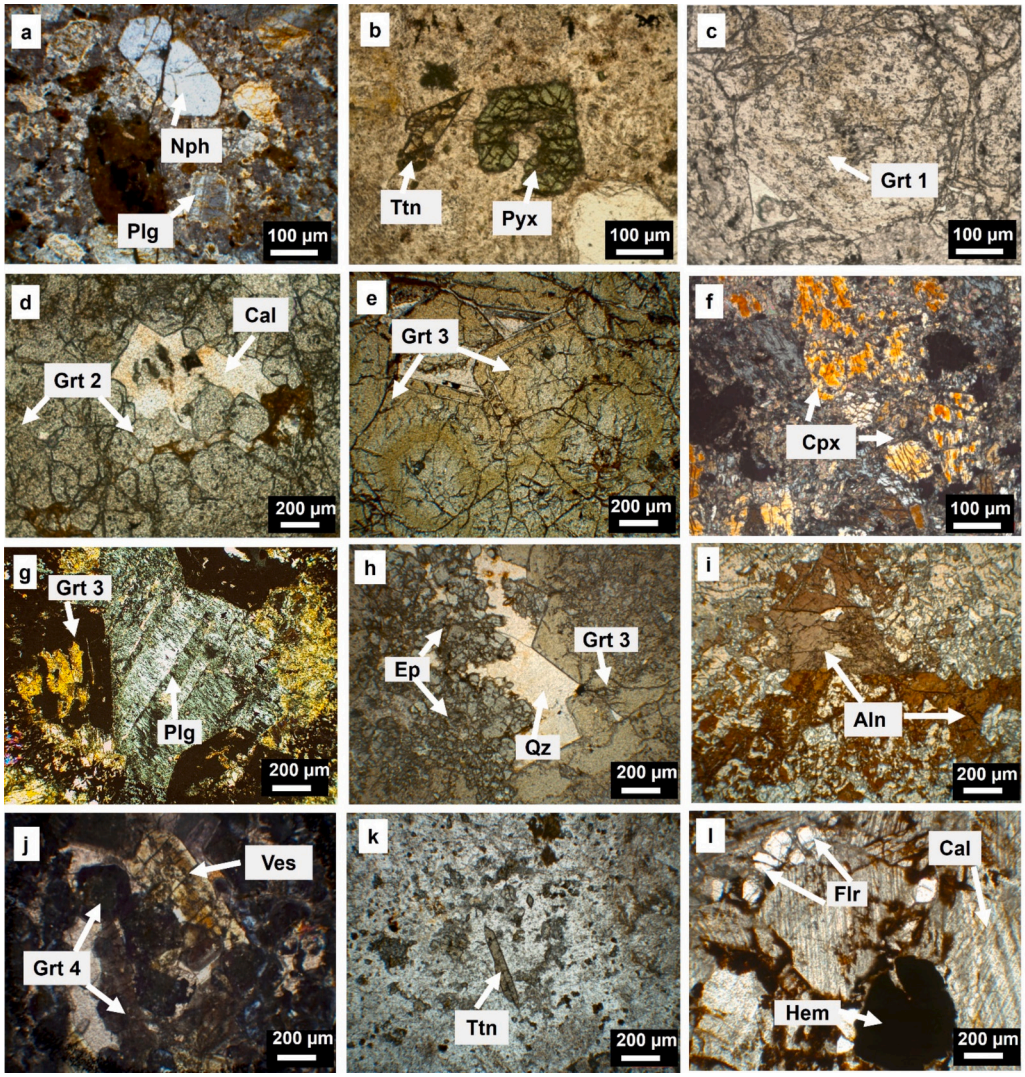

Fig. 5. Photomicrographs of the mineral assemblages and their textural properties in the (a, b) Keban Magmatics, (c, d, e, f, g, h) endoskarn zone, (i, j) exoskarn zone, (*k*,*l*) calcic exoskarn zone. a. euhedral nepheline and plagioclase, b. subhedral brown titanite and light green colored pyroxene, c. Grt 1 euhedral grossular, d. fine-grained Grt 2 Fe-rich grossular, e. Grt 3 andradite showing oscillatory zoning, f. clinopyroxene with significant unidirectional cleavages, g. Grt 3 replaced by amphibole from its core overprinting plagioclase, h. andradite replaced by epidote accompanied by euhedral epidote and quartz, i. brown allanite replacing garnet, j. isotropic Grt 4 garnet and tabular prismatic vesuvianite with olive green interference color, k. prismatic titanite in association with Grt 4, l. fluorite, calcite and hematite in the calcic exoskarn zone (Nph: nepheline; Plg: plagioclase; Ttn: titanite; Pyx: pyroxene; Cpx: clinopyroxene; Grt: garnet; Cal: calcite; Ves: vesuvianite; Ep: epidote; Aln: allanite; Phl: phlogopite, Flr: fluorite; Qz: quartz; Hem: hematite). (For interpretation of the references to color in this figure legend, the reader is referred to the web version of this article.)

sulfosalts, native gold, scheelite and pyrrhotite, with gangue minerals of epidote, chlorite, fluorite, calcite, and quartz. The supergene alteration is represented by hematite, goethite, copper minerals (chalcocite and covellite), malachite, rhodochrosite and pyrolusite. Sulfide-rich parts generated manganese oxide-rich gossans that are related to Pb—Zn skarns at or near the surface. In addition, calc-schists with thicknesses up to 15 m in the Keban area contain layered Ag-bearing manganese oxide mineralization. On the other hand, in a number of underground galleries we recognized a disseminated vein-sulfide mineralization developing within the calcschist-limestone contact. These massive sulfide veins cut some of ore-bearing skarn zones (Fig. 4j, k). The Keban fluorite mineralization, part of a metallogenic province in the east-central Anatolia, is hosted by Palaeozoic dolomitic marble and calcschist adjacent to an alkaline intrusion. The mineralization is emplaced as stockwork and vein-type bodies with overlapping lenses, which strike broadly north-south and dip eastward, with individual veins extending up to 30 m in length and 0.9 m in thickness (Öztürk et al., 2019). An estimate of the ore resource is 0.053 Mt. of indicated, 0.1 Mt. of inferred, and 0.034 Mt. of measured fluorite ore (MTA, 1989). The fluorite veins cut the skarn mineralization and contain gangue of quartz, calcite, mica and epidote (Fig. 4l).

5.2. Skarn petrography

The garnets vary between green to light-dark brown, small anhedral isotropic or large, and oscillatory-zoned (Fig. 5c-e, g, h, j). The composition of garnets ranges from grossular to andradite in the endoskarn zone and is dominated by grossular in the exoskarn zone. Garnets are numbered systematically according to their abundance from endoskarn to exoskarn. Grt 1 grossular is euhedral and encountered together with clinopyroxene in the endoskarn zone (Fig. 5c). It is partly replaced by epidote and the spaces among the grains are filled with calcite and quartz. Fe-rich grossular garnets (Grt 2) are fine to medium grained and composed of clinopyroxene and calcite (Fig. 5d). Grt 3 is represented by medium to coarse-grained andradite showing oscillatory zoning (Fig. 5e) and is accompanied by subhedral clinopyroxene (Fig. 5f),

Table 1
Petrographic characteristics of skarn formations in the study area.

Rock type	Sample No.	Mineral facies	Mineral assemblage	Characteristic properties
Endoskarn	B-KS3–1; B-KS3–7; B-KS3–4-(1)(2); B-KS3–4-2; D-KS1–7; D-KS1–9; KS-17-50; KS-17-61; KS-17-62; KS-19-9KS-19-8	Gr-Pyx-Plg skarn	Gr (Adr and Grs) + Pyx (Di) + Plg (Alb) ± Ort± Ep ± Flg ± Bio ± Mus ± Qtz ± Ti ± Trm ± Cal ± Aln ± Chl ± Hm	It occurs at alkali syenite porphyry contact as a thin zone or veinlet. Coarse-grained garnets with zonation are replaced by epidote, allanite and calcite. Calcite and quartz fill the open cavities.
Exoskarn	A-KS1–5; B-KS2–1; B-KS2–2; B-KS3–8; D-KS2–4	Pyx skarn	Pyx (Di) + Mus ± Bio ± Ep ± Qz ± Flr	Developed closer to meta-sedimentary rocks. Coarse-grained calcites with long needle-like pyroxene are cut by quartz and calcite veins.
	C-KS2–5; D-KS2–5; KS-17-13	Gr-Pyx skarn	Gr (Grs) + Pyx +Cal ± Ort ±Ep ± Mus ± Phl ± Trm	Garnets are replaced by calcite.
	C-KS1–2; D-KS1–10; D-KS2–1	Ve-Pyx-Gr skarn	Ve + Gr (Grs) + Pyx+ Cal ± Ep ± Mus	Garnet and vesuvianite alternate with calcite. Fine-grained pyroxenes replace garnet and calcite.
	B-KS3–5-(2); B-KS3–6; KS-17-17; KS-17-53	Ve-Gr skarn	Ve + Gr (Grs) + Cal ± Ep	Garnets are replaced by calcite.
	A-KS1–3; A-KS1–3-(2); A-KS1–4; A-KS1–6; A-KS1–7-(1); A-KS1–7-(2); Sample 1; B-KS1–3; B-KS2–6-(1); B-KS2–6-(2); B-KS2–7; B-KS2–8; C-KS2–4-1; C-KS2–4-2; C-KS2–4; C-KS3–2;C-KS3–3; C-KS4–1; C-KS4–2; C-KS4–4-1; C-KS4–4-2; C-KS4–5; D-KS1–1; D-KS1–2; D-KS1–3; D-KS1–4; D-KS1–5-1; D-KS1–5-2; D-KS1–6; D-KS2–6; D-KS2–7; D-KS2–8; KS-17-59; KS-17-57; KS-19-6	Gr skarn	Cal + Gr (Grs) + Mus ± Pyx ±Phl ± Flr ± Hm ± Ccp ± Gn ± Sp	Medium to coarse-grained calcites with polygonal shapes are located with garnet, muscovite, fluorite, phlogopite, and hematite. It contains ore-bearing calcite and quartz veins.

Pyx, pyroxene; Gr, garnet; Grs, grossular; And, andradite; Di, diopside; Qz, quartz; Plg, plagioclase; Ve, vesuvianite; Cal, calcite; Ti, titanite; Ort, orthoclase; Bio, biotite;
Mus, muscovite; Phl, phlogopite; Chl, chlorite; Trm, tremolite; Aln, allanite; Ep, epidote; Flr, fluorite; Sp, sphalerite; Gn, galena; Ccp, chalcopyrite; Mag, magnetite; Hm, hematite.

plagioclase (Fig. 5g), epidote (Fig. 5h), and allanite (Fig. 5i). They were developed by overprinting on plagioclase in the endoskarn zones and these features suggest that garnet formed after plagioclase (Fig. 5g). Some of them are replaced by amphibole, epidote and allanite (Fig. 5g-i). In the exoskarn zone, Grt 4 grossular dominated garnets attaining a length of 200 to 300 μm overprint on rod-like, prismatic, and tabular vesuvianites only observed in this zone (Fig. 5i), and occur in association with sericite, fine-grained pyroxenes, prismatic titanite (Fig. 5k), and quartz.

In the endoskarn zone, clinopyroxene is generally subhedral, with a second-order interference color and replaced by amphibole (Fig. 5f). The epidote, calcite and sericite have formed as alteration product of clinopyroxene, garnet and plagioclase (Fig. 5g, h). The actinolite derived from the pyroxene was a result of Fe loss and the enrichment of Ca. Chlorite was commonly observed to overprint the clinopyroxene and/or epidote. Fractures and vugs among the skarn minerals were mostly filled by fine grained calcite and quartz (Fig. 5d, h). Hematite with magnetite relicts and fine to medium grained fluorite are commonly observed on coarse-grained calcite in the calcic exoskarn (Fig. 5l).

5.3. Ore petrography

Ore minerals in Keban skarn deposit develop mainly as vein and/or disseminated, and massive forms with variable grain sizes, from fine to very coarse. Massive sulfides are composed primarily of coarse to medium grained porous and euhedral pyrite and marcasite. They cut pyrite-calcite veins at ~400 m depths (Fig. 4j).

Vein and/or disseminated mineralization has different types of ore minerals reflecting the characteristics of ore-bearing fluids. They mainly occur as a replacement texture with skarn calcite in limestones. The deposit contains three different forms of sphalerite. Anhedral, dark brown colored Sphalerite-I contains pyrite inclusions and chalcopyrite exsolutions (Fig. 6a). Yellowish-light brown colored Sphalerite-II is intergrown with anhedral galena-I and has sulfosalts and chalcopyrite-II (Fig. 6b, e). Medium-brown colored Sphalerite-III is composed of medium-coarse grained subhedral sphalerites. They are accompanied by colloform and framboidal pyrite-III and marcasite (Fig. 6c) and are encapsulated by galena-II (Fig. 6d) representing the paragenetically latest phase of sphalerite precipitation.

Chalcopyrite-I within sphalerite-I, bar- or bleb-like chalcopyrite grains are arranged irregularly, so called chalcopyrite disease (e.g., Barton and Bethke, 1987) (Fig. 6a). Chalcopyrite-II observed as exsolutions in Sphalerite-II and are associated with sulfosalts (Fig. 6e). Chalcopyrite-III is accompanied by pyrite-I and II and magnetite-II and hosts covellite within their relicts.

Magnetite-I is generally euhedral and occurs between the sphalerite-I crystals indicating that their formation postdates sphalerite-I (Fig. 6f). Limonite occurs as fine to medium grains. Magnetite-II crystals are partly or completely converted to hematite and limonite and are accompanied by pyrite-I and II and chalcopyrite-III and quartz (Fig. 6g).

Pyrite also has three styles of occurrence. Pyrite-I is represented by euhedral and subhedral, medium to coarse-grained crystals and some grains show cataclastic texture (Fig. 6f) whereas pyrite-II has a porous texture and associated with fibrous pirolusite (Fig. 6i). They are associated with chalcopyrite-III, sphalerite-I, arsenopyrite, pyrrhotite, marcasite, magnetite, hematite, covellite, limonite, and rare amount of native gold (Fig. 6f-i). Anhedral fine to medium grained pyrite-III with colloform and framboidal texture occurs between sphalerite-III and galena-II (Fig. 6c). Colloform texture in the pyrite-III indicates that crystallization occurred from the supersaturated ore-bearing hydrothermal fluid due to a sudden change in the physico-chemical conditions in the shallow subsurface environment (e.g. Ren and Yundeng, 2006).

The presence of covellite, marcasite, limonite, goethite with the

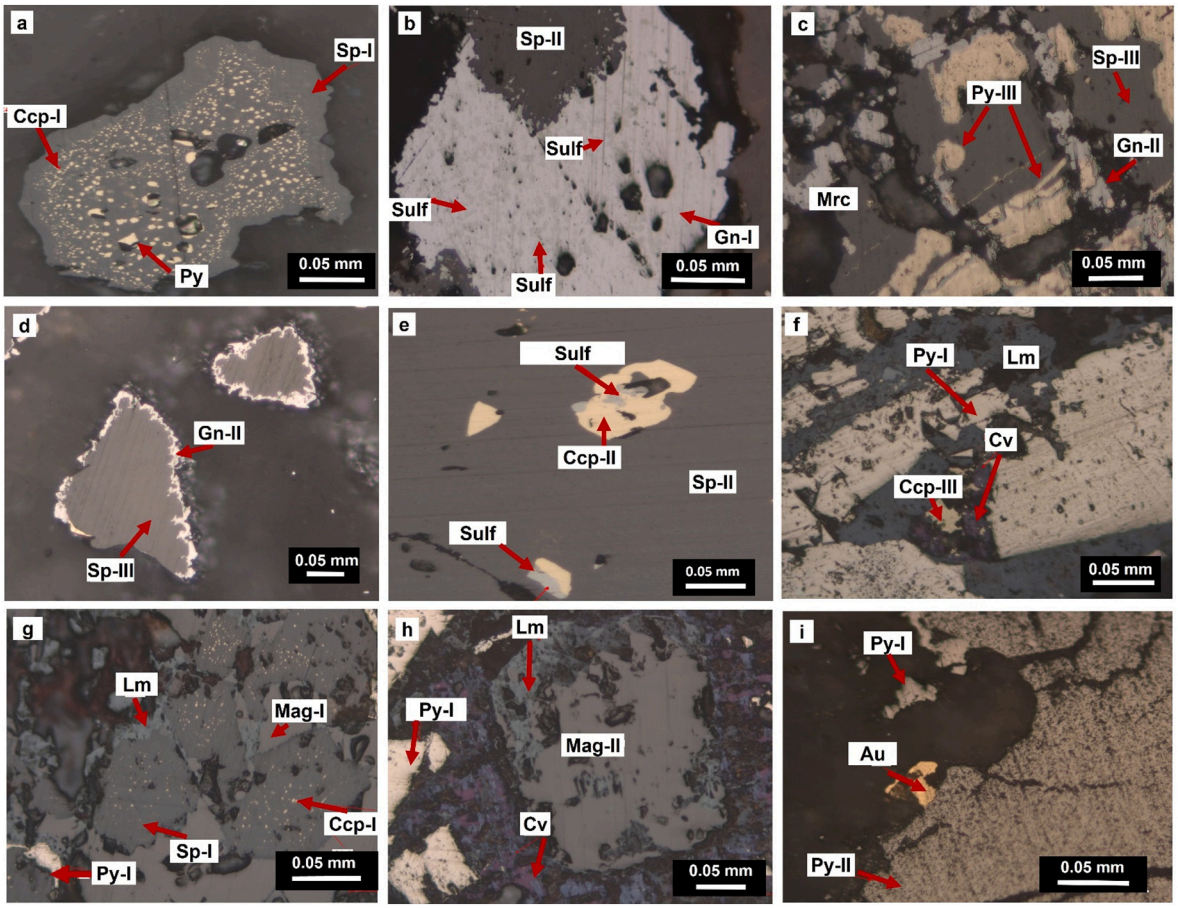

Fig. 6. a. sphalerite-I grain with chalcopyrite-I showing chalcopyrite disease and pyrite inclusions, b. sulfosalt exsolution within galena-I and sphalerite-II, c. colloform-like pyrite-III with sphalerite-III and galena-II, d. sphalerite-III are encapsulated by galena-II, e. euhedral chalcopyrite-II exsolutions and sulfosalts within sphalerite-II, f. chalcopyrite-III accompanied by pyrite-I and covellite within their relicts, g. magnetite-I and limonite surrounding sphalerite-I with chalcopyrite-I and subhedral pyrite-I, h. limonite and covellite that formed by alteration of magnetite-II, pyrite-I and chalcopyrite-III, i. euhedral pyrite-I and porous pyrite-II with native gold; (Sp, sphalerite; Gn, galenite; Pr, pyrite; Sulf, sulfosalt mineral; Ccp, chalcopyrite; Lm, limonite; Mag, magnetite; Cv, covellite; Au, native gold). (For interpretation of the references to color in this figure legend, the reader is referred to the web version of this article.)

carbonate minerals (e.g. smithsonite and rhodocrosite), iron and manganese oxides at the shallow depths and their textural relations are indicative of a supergene alteration. Based on the nature of hydrothermal alteration, mineral assemblage, and crosscutting relationships, the Keban mineralization is divided into prograde skarn (Stage I), retrograde skarn-sulfides (Stage II), and supergene stage (Stage III), (Supplementary Fig. S2).

6. Analytical techniques

To examine the skarn zones, eighty-five samples were collected systematically from the host rocks and alteration zones between Yahyalı and Palubaş districts (Supplementary Fig. S1). Ore and rock samples from drill cores were selected considering the distribution of skarn and ore mineral assemblages (Supplementary Table T2). For the mineral chemistry analysis, thin sections were prepared at the thin section laboratory of the Geology Department of Ankara University, and petrographical descriptions were made using a Leica DM/LSP brand polarizing microscope. Polished sections of selected samples were prepared at the Earth Sciences Application and Research Center of Ankara University (YEBIM) and studied with a Leitz Ortholux brand ore microscope.

Polished wafers of ore and skarn minerals were carbon coated at the YEBIM laboratory. Microprobe analysis of garnet, pyroxene and vesuvianite was carried out at the same laboratory using a JEOL JXA–8230 device with 15 kV accelerating voltage, a beam current of 1.5×10^{-8} nA, and a beam size of 5 μm. Microprobe analysis of sulfide minerals was conducted at the Camborne School of Mines laboratory of the University of Exeter using a JEOL JXA-8200 super probe device with 15 kV accelerating voltage and a beam current of 1.8×10^{-7} nA and beam spot of 10 μm. Data reduction of silicate minerals followed the ZAF software provided by JEOL, whereas that of sulfide minerals followed the phi-rho-Z routine provided by JEOL.

Doubly-polished wafers (200-μm thickness) prepared from fluorite, garnet, pyroxene, quartz, and calcite were used for microthermometric determinations. Fluid inclusion (FI) analysis was carried out using a Linkam THMSG-600 brand freezing-heating stage installed on a Leica DM 2500 M polarizing microscope at the FI laboratory of the Geology Department of Ankara University. Inclusion types were petrographically determined before the measurements. The temperature range of the stage is from −150 to 600 °C. The stage was calibrated with pure synthetic H_2O and H_2O-NaCl FI standards. The accuracy of the homogenization temperature is ±0.4 °C for heating experiments and ± 0.2 °C for cooling experiments.

Calcite samples for carbon and oxygen isotope analyses were powdered under 200-mesh size using Fritsch mill and 10 g was used for the analysis. $\delta^{18}O$ and $\delta^{13}C$ of calcites were measured using an automated carbonate preparation device (KIEL-III) coupled to a gas ratio mass spectrometer (Finnigan MAT 252) at the Environmental Isotope Laboratory of the University of Arizona (USA). Powder samples were reacted with dehydrated phosphoric acid at 70 °C. The isotope ratio measurement is calibrated based on repeated measurements of

international standards NBS-19 and NBS-18 and analytical precision is ±0.1 ‰ (VSMOW) for $\delta^{18}O$ and ± 0.08 ‰ (VPDB) for $\delta^{13}C$ (1σ).

Sulfide minerals for sulfur isotope analysis were handpicked under a binocular microscope. $\delta^{34}S$ analysis was conducted on SO_2 gas using a continuous flow isotope ratio mass spectrometry device (ThermoQuest Finnigan Delta PlusXL) at the Environmental Isotope Laboratory of the University of Arizona. Samples were combusted at 1030 °C by oxygen gas and V_2O_5 with an element analyzer coupled to the mass spectrometer. The standardization was made by OGS-1 and NBS-123 international standards and comparing sulfide and sulfate materials from different laboratories. The calibration is between −10 and + 30 per mil and analytical precision is ±0.15 ‰ (CDT).

7. Mineral chemistry

7.1. Silicates

7.1.1. Garnet and pyroxene

Chemical compositions and end-member calculations of garnet and pyroxene from endoskarn and exoskarn zones are shown in Supplementary Tables T3 and T4, respectively. The grossular content of garnets is in the range of 2.4 to 90.4 mol% and andradite abundance is up to 91.6 mol%. Total pyrope, almandine and spessartine contents of garnets are less than 20.8 mol% and most belong to the grossular–andradite solid solution series (Fig. 7).

Garnets from stage I and II have compositions of $Adr_{3.22–94.62}$ $Grs_{2.39–90.04}$ $Prs_{3.57–20.51}$ and Adr $_{3.94–70.59}$ $Grs_{16.05–79.67}$ $Prs_{9.74–22.61}$, respectively (Prs = pyralspite = pyrope+spessartine+almandine). The composition of stage I garnets extends from andradite to grossular corner and stage II garnets are almost equally clustered around the

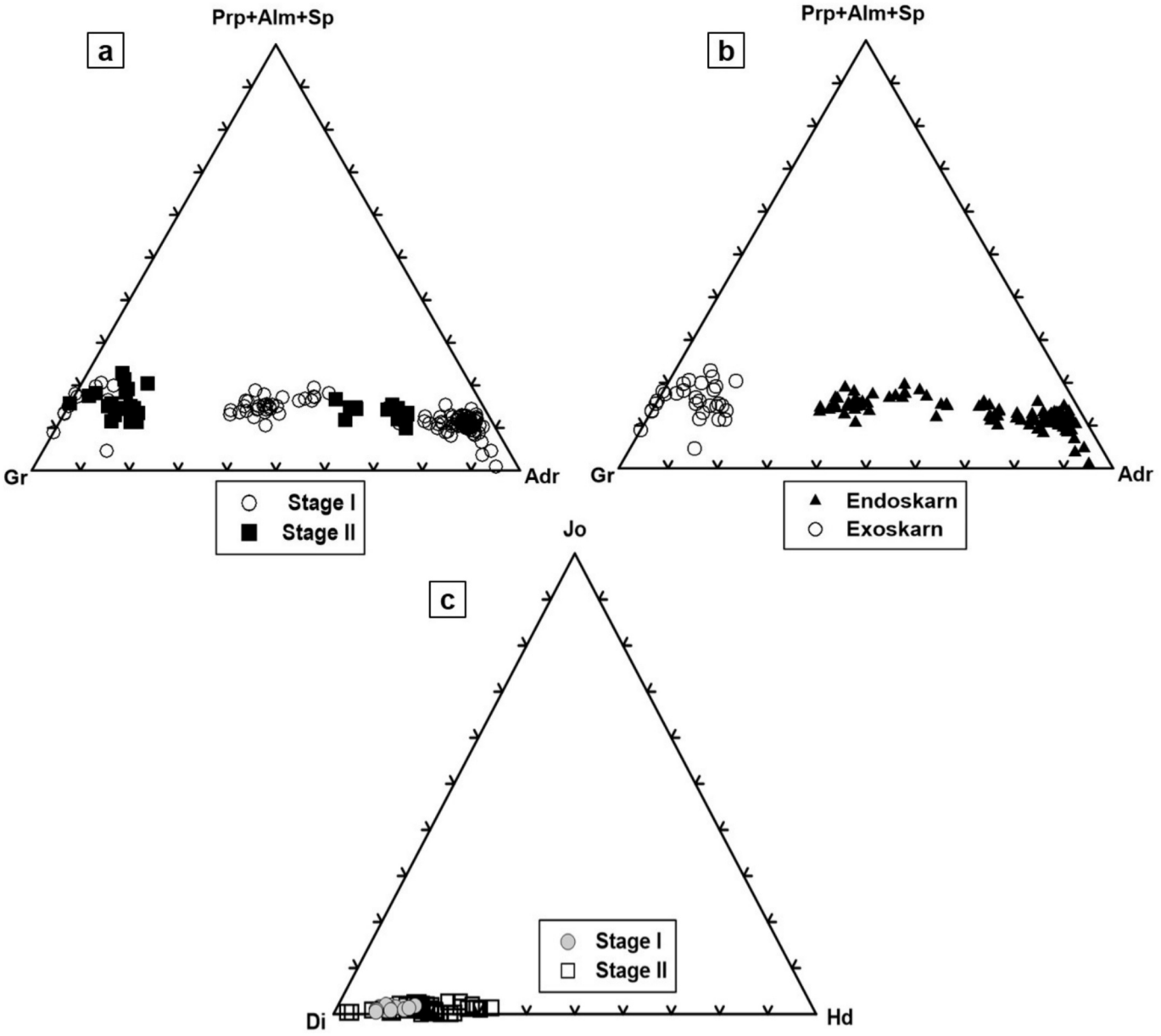

Fig. 7. a. Variations in the chemical composition of garnets from stages I and II, b. chemical composition of garnets from endoskarn and exoskarn, c. chemical composition of pyroxenes from stages I and II (Gr: Grossular, Adr: Andradite, Prp: pyrope, Sps: Spessartine, Alm: Almandine, Di: Diopside, Hd: Hedenbergite, Jo: Johannsenite).

grossular end-member (Fig. 7a). Garnets of the endoskarn zone are generally in andradite-grossular composition (Adr $_{17.77–94.62}$ Grs$_{2.39–67.90}$Prs$_{3.57–19.28}$) (Fig. 7b). The concentrations of SiO_2, Al_2O_3, CaO, MnO and FeO of garnet in the endoskarn zone are 34.77–39.82 wt %, 0.54–15.07 wt%, 29.04–32.21 wt%, 0.13–1.13 wt% and 9.77–31.98 wt%, respectively. Grossular dominated-Grt 1 contains significant amount of Al (Adr $_{17.77–23.76}$ Grs$_{63.29–67.90}$ Prs$_{10.33–12.88}$). Grt 2 and Grt 3 are more enriched in Fe with Adr $_{34.06–50.88}$ Grs$_{29.62–50.48}$ Prs$_{10.53–19.28}$ and Adr $_{53.44–94.62}$ Grs$_{2.39–16.05}$ Prs$_{3.57–16.55}$, respectively. Whereas Fe-rich grossular-Grt 2 shows strong oscillatory zoning in Al and Fe^{3+} and increases in Ca and Mn concentrations at the rims. Andradite-dominated-Grt 3 has higher Fe^{3+} contents, weak oscillatory zoning in Al and Fe^{3+} and increases in Ca contents at the rims. Garnets with Fe-rich rims and Al-rich cores are common in the oscillatory garnets (Supplementary Table T3).

Garnets (Grt 4) of the exoskarn zone are grossular-rich (Adr $_{0.68–15.58}$ Grs$_{70.50–90.44}$ Prs$_{4.60–17.55}$) and accompanied by vesuvianite (Fig. 7b). They have SiO_2, Al_2O_3, CaO, MnO and FeO contents of 38.06–42.54 wt %, 13.60–21.36 wt%, 29.94–34.49 wt%, 0.23–1.05 wt% and 2.73–11.04 wt%, respectively. These garnets generally have higher Al_2O_3 and SiO_2 but lower FeO contents than those of the endoskarn zone. In addition, they have weak oscillatory zoning in Al, Fe^{3+} and Fe^{2+} and show an increase in Fe^{3+} at the rims. Unlike the endoskarn zone, Ti concentration (0.11–1.96 wt%) is relatively high (Supplementary Table T3).

Pyroxenes of endoskarn are in clinopyroxene composition with Hed$_{2.64–15.96}$ Dio$_{70.23–90.76}$ Joh$_{0.31–2.65}$ (Fig. 7c). Clinopyroxenes in garnet-pyroxene skarn of stage I are diopside-rich, whereas composition of pyroxenes in stage II ranges from diopside to hedenbergite. The pyroxene in stage II has high FeO (3.7–11 wt%) TiO_2 (0.03–0.53 wt%), and Al_2O_3 (0.7–7.5 wt%) compared to stage I samples (FeO = 2.7–4.6 wt%; TiO_2 = 0–0.04 wt%; Al_2O_3 = 1.5–2.1 wt%) (Supplementary Table T4). In stage I, most of iron and magnesium were trapped within diopside. Chemical compositions of studied garnets plot into the Zn field (Supplementary Fig. S3a) and those of pyroxenes fall into the Cu field (Supplementary Fig. S3b).

7.1.2. Vesuvianite

The typical formula of vesuvianite is $X_{19}Y_{13}Z_{18}T_{0-5}O_{68}W_{10}$, where X stands for Ca, Na, REE, Pb^{2+}, Sb^{3+}; Y=Al, Mg, Fe^{3+}, Fe^{2+}, Ti^{4+}, Mn, Cu, Zn; Z = Si; T = B; and W = OH, F, O^{2-}. F can be noted in concentrations of up to 3.2 wt% (Groat et al., 1992). Vesuvianite from the Keban exoskarn is characterized by Al-rich compositions (8.5–10.6 apfu) and relatively high F (1.0–1.6 wt%). Si contents are high (38–40 wt%, 20.1–20.9 apfu) indicating that Al incorporation in the tetrahedral position is limited. Fe is primarily in the +3 oxidation state (1.47–2.32 apfu) (Groat et al., 1992). Mg content varies from 1.6 to 3.7 apfu and Mn is lower (0.04–0.09 apfu) (Supplementary Table T5).

7.2. Sulfides

A total of 54 points were analyzed (21 in sphalerite, 18 in galena, 12 in chalcopyrite, and 3 in pyrite) on three ore samples. Results of trace element analysis of sulfides are summarized in Supplementary Table T6 and illustrated in Fig. 9.

7.2.1. Sphalerite

Sphalerite shows significant variation in Fe from 0.1 to 8.7 wt%. Sphalerite-I is represented by 3.11–8.72 wt% Fe, 50–61.2 wt% Zn, low Ag (<0.05 wt%), relatively high Cu (0.14–7.25 wt%), and plots to the high to intermediate Fe-sphalerite fields. Sphalerite-II contains 0.06–2.93 wt% Fe, 63.1–65.4 wt% Zn, 0.09–0.18 wt% Ag, low Cu (<0.46 wt%) and might be classified as Fe-poor sphalerite (Figs. 8 and 9). In addition, they have low Mn (0.2–1.0 wt%), Cd (0.09–0.4 wt%), As (0–0.6 wt%), and moderate Ga (0.05–0.17 wt%) compositions accompanied by very low Co, Ni, In, and Sb contents (Supplementary Table T6).

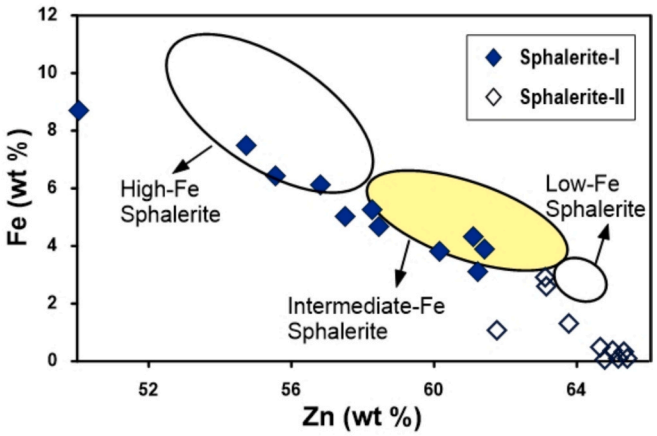

Fig. 8. Binary plot of varying Fe composition in sphalerite. Field for sphalerite composition from Raza et al. (2020).

7.2.2. Galena

Major element compositions of galena-I are as follows: S: 13.64–17.05 wt%; Pb: 62.35–80.79 wt%; Zn: 0–0.2 wt%. Although it has the highest Hg (0.6–0.8 wt%), Sb (0.17–9.9 wt%) and Ag (0.045.03 wt %) concentrations, Fe, Mn, Co and Ni contents are quite low (Fig. 9). High Hg, Sb, Ag, Cu (<1.2 wt%) and As (<4.6 wt%) concentrations of galena coincide with the existence of tetrahedrite-tennantite and Cu—Pb sulfosalt inclusions (e.g., Cook et al., 2009).

7.2.3. Chalcopyrite

Chalcopyrites have the following element compositions: S: 34.9–35.8 wt%; Fe: 29.5–30.8 wt%; Cu: 33.75–35.05 wt%; Pb: 0.10–0.14 wt%; Hg: 0.19–0.49 wt%. They have low Zn, Mn, As, and Ag concentrations. Although chalcopyrite-I is distinctive with relatively high Zn content (0.05–0.14 wt%), concentrations of other elements are similar to chalcopyrite-II (Supplementary Table T6).

7.2.4. Pyrite

Element compositions of pyrite-I are as follows: S: 51.5–53.6 wt%; Fe: 44.9–46.8 wt%; Cu: 0–0.07 wt%; Pb: 0.16–0.24 wt%; As: 0.02–0.05 wt%; Hg: 0.19–0.32 wt%. Pyrites have low Zn, Ag, Ni and In contents (Fig. 9) (Supplementary Table T6).

8. Fluid inclusion (FI) studies

8.1. Inclusion types and petrography

The FI types in the Keban deposit are simple to identify in all host minerals from each stage. They are hosted in garnet in stage I, and garnet, epidote, fluorite, and quartz in stage II, and quartz, fluorite, and calcite in fluorite+pyrite+quartz+calcite vein. Fluid inclusions of Stage II are associated with the disseminated sphalerite, galena and molybdenite and chalcopyrite, sphalerite, hematite, and pyrite clusters. The results of the measurements are given in Table 2. Before freezing-heating measurements, FIs in each crystal were petrographically described. FIs were examined on the twenty-double-polished wafers, according to the criteria reported by Roedder (1984) and Van den Kerkhof and Hein (2001). Since gas phases trapped in LV-type inclusions are mostly composed of H_2O, the salinity was estimated with respect to the NaCl-H_2O system (Bodnar and Vityk, 1994).

VL-type FIs were defined as primary liquid- and vapor-bearing two-phase inclusions (L + V) with vapor-rich phase contents (V > L). These inclusions homogenized into the gas phase and. Were identified in stage II quartz and garnet. LV-type FIs are primary two-phase inclusions (L +

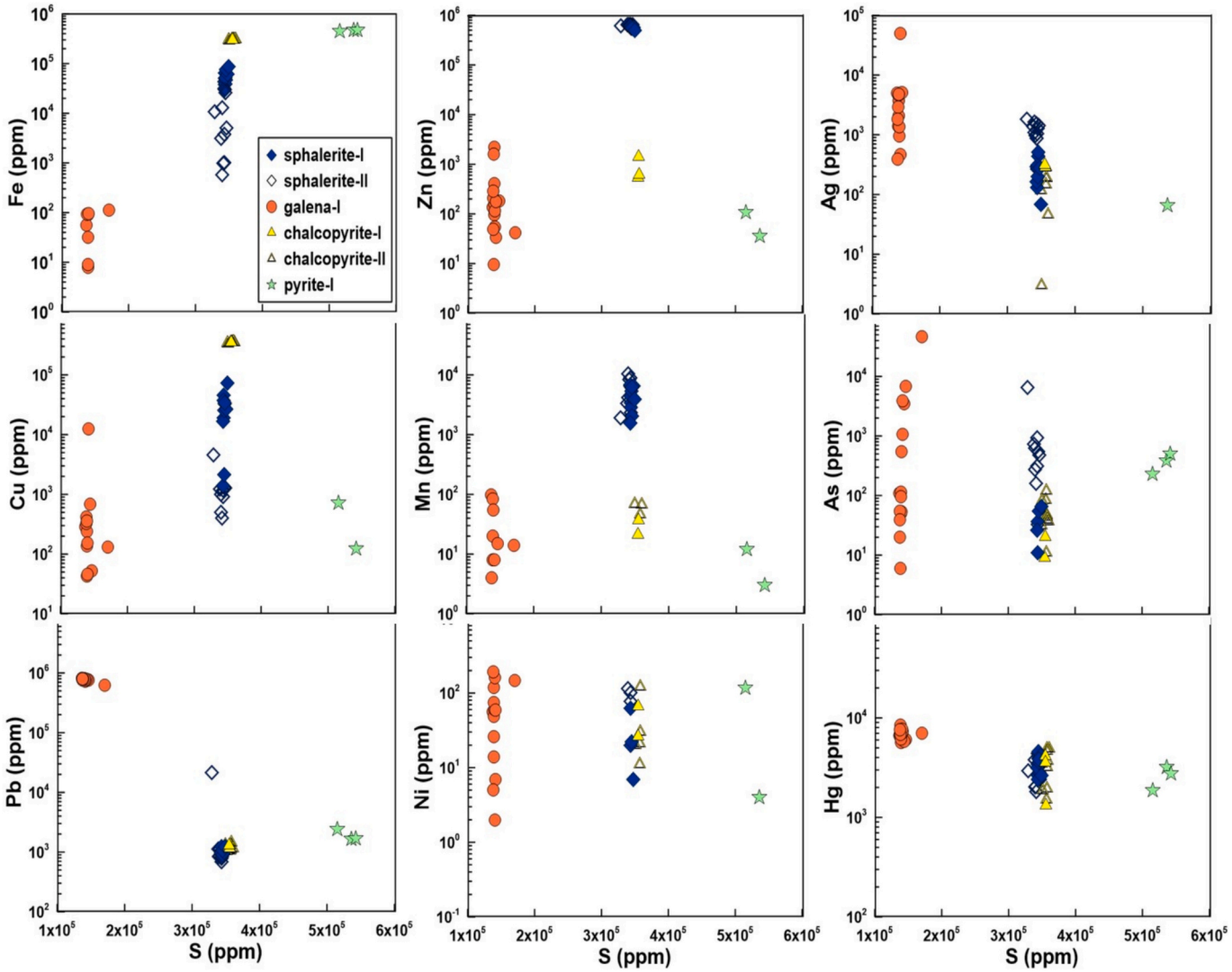

Fig. 9. Elemental compositions vs. S contents for sulfides of the Keban Pb—Zn skarn deposit.

V) with liquid-rich phase contents (L > V). These inclusions homogenized into the liquid phase. Two-phase primary inclusions are commonly irregular, elongated, circular, and have negative crystal shapes. LV-type FIs were identified in almost all minerals. However, VL-type inclusions are only accompanied by LV-type inclusions in stage II garnet and quartz.

Garnet inclusions of stage I are LV-type and their size varies from 5.2 to 10.2 μm. Stage II garnets contain LV-type -dominated and vapor-rich VL-type inclusions (up to 18 μm) (Fig. 10a). LV-type inclusions recorded in epidote are generally small size (5–6.6 μm) and belong to stage II. Quartzs of this stage contain commonly LV-type (Fig. 10b) and VL-type inclusions. Small to medium LV-type inclusions (5.3–11.2 μm) are generally observed in fluorite. In fluorite+pyrite+quartz+calcite vein, large LV-type inclusions (up to 28.9 μm) are generally observed in fluorite (Fig. 10c) and quartzs and calcites (Fig. 10d) are identified as small and medium-sized (5–13.2 μm) LV-type inclusions.

8.2. *Microthermometric results*

Homogenization temperatures and wt% NaCl equivalent salinity ranges of measurements are given in Table 2. Homogenization temperatures recorded in primary inclusions of stage I garnets are 473 to 572 °C (Fig. 11a) (Table 2). Homogenization temperatures measured in VL-type inclusions of stage-II garnets (382–384 °C) are relatively lower than those of LV-type garnet (387–524 °C)(Fig. 11b). VL-type inclusions in stage II quartz are represented by relatively a narrow temperature range from 410 to 496 °C whilst LV-type inclusions in stage II quartz, epidote and fluorite yielded a wide temperature range from 254 to 520 °C, from 230 to 421 °C and from 317 to 419 °C, respectively (Fig. 11b). In fluorite+pyrite+quartz+calcite vein, temperatures of LV-type fluorite (244–452 °C) are relatively higher than those of LV-type calcite (212–421 °C) and LV-type inclusions of stage II fluorites (317–419 °C) (Table 2). Temperatures measured in LV-type inclusions of the vein quartzs (279–503 °C) are relatively lower than thoseof stage II quartz (254–520 °C) (Fig. 11c) (Table 2).

Similar homogenization temperatures recorded in liquid- and gas-phase inclusions in a mineral might be indicative of boiling (Bodnar, 2003). Boiling in ore-bearing solutions may be intermittent and temperature and salinity are periodically increased (Kwak, 1986). However, boiling is a common process at shallow zones of skarn systems and mostly postdates the formation of a low-temperature phase. The occurrence of boiling in skarns does not necessitate a pressure correction for the homogenization temperatures (Roedder, 1979). Compared to other skarn types, the solutions in Pb—Zn skarns are often more diluted (<30 wt% NaCl) (Kwak, 1986) and ore formation likely occurred from the low-salinity magmatic fluid although Pb and Zn concentrations are highest in the early brine and and vapor inclusions (Baker et al., 2004). At high temperatures, fracturing by hydrothermal fluids promotes

Table 2
Microthermometric fluid inclusion data from garnet, epidote, quartz, fluorite and calcite minerals of Keban skarn.

Stage	Mineral	Sample no	FI Type	Homogen. modes	FI Size (μm)	Statistical parameters	First melting temperature (Te, °C)	Last melting temperature (Tm_{ice}, °C)	Homogenization temperature (Th, °C)	Salinity (wt% NaCl eq.)
Stage-I	Garnet	B-KS3–1,D-KS1–10, KS-19-8	LV-type	Liquid	5.2–10.2	Max	−38.2	−8.9	572, Th_L	11.9
						Min	−26	–	473, Th_L	–
						n	2	1	4	1
Stage-II	Garnet	D-KS1–7, D-KS1–10, KS-19-9	VL-type	Vapor	5.3–13.2	Max	−32	–	384, Th_V	–
						Min	–	–	382, Th_V	–
						n	1	–	2	–
			LV-type	Liquid	6.3–18	Max	−24	−2.7	524, Th_L	4.4
						Min	−19	−1.4	387, Th_L	2.4
						n	3	3	5	3
	Epidote	KS-17-61, KS-18-23	LV-type	Liquid	5–6.6	Max	−34	−3.8	421, Th_L	6.1
						Min	−24	−1.4	230, Th_L	2.4
						n	5	5	5	5
	Quartz	KS-17-61, KS-18-20, KS-18-23, KS-19-6	VL-type	Vapor	7–15	Max	−27	−1.2	496, Th_V	2.1
						Min	−23.1	−0.5	410, Th_V	0.8
						n	2	2	2	2
			LV-type	Liquid	5–20.9	Max	−46.2	−4.2	520, Th_L	6.6
						Min	−0.5	−0.5	254, Th_L	0.8
						n	35	35	46	35
	Fluorite	KS-19-6	LV-type	Liquid	5.3–11.2	Max	−33	−4	419, Th_L	6.3
						Min	−21	−1	317, Th_L	3.4
						n	4	4	4	4
Florite+pyrite+quartz+ calcite vein	Quartz	KS-18-22, KS-18-24	LV-type	Liquid	5.1–12.8	Max	−46	−4.3	503, Th_L	6.9
						Min	−13.6	−0.2	279, Th_L	0.3
						n	11	11	12	11
	Fluorite	KS-17-44, KS-17-59, KS-18-19, KS-18-24	LV-type	Liquid	5–28.9	Max	−45.4	−9.1	452, Th_L	12.1
						Min	−8	−0.5	244, Th_L	1.5
						n	24	24	24	24
	Calcite	KS-17-44, KS-19-13	LV-type	Liquid	5–13.2	Max	−32.7	−9.2	421, Th_L	12.2
						Min	−11	−1.2	212, Th_L	2.1
						n	20	20	24	20

boiling and allows meteoric water infiltration that cools the system, and as a result, temperature and salinity are decreased (Kwak, 1986). In sample KS-18-20 of stage II, boiling was recognized in coexisting liquid-rich and vapor-rich (L + V) inclusions of quartz, which is adjacent to chalcopyrite and pyrite. The VL-type fluid inclusion in quartz that homogenized to the vapor phase had a homogenization temperature from 410 to 496 °C and the salinities between 0.8 and 2 wt% NaCl eq. Th of LV-type inclusions, which homogenized to liquid phase and coexist with VL-type inclusions in quartz, is between 395 and 482 °C with 4.4 to 6.4 wt% NaCl eq salinities. The coexistence of both type inclusions in the same fluid, with the similar Th values, clearly indicated a boiling assemblage for both types (Bodnar et al., 1985).

Salinity in primary inclusions of stage-I garnets is 11.9 wt% NaCl eq. (Fig. 11d) and decreases to 4.4–2.4 wt% in stage II garnets (Fig. 11e). Salinities of stage II in descending order are from garnets to epidote (6.1–2.4 wt%) (Fig. 11e). LV-type inclusions of stage II fluorites have salinities (3.4–6.3 wt%) similar to LV-type quartz and epidote. The salinity in LV-type inclusion of the fluorite+pyrite+quartz+calcite vein fluorites (12.1–1.5 wt%) and calcites (12.2–2.1 wt%) are higher than those of LV-type quartz (6.9–0.3 wt%) (Table 2; Fig. 11f).

The eutectic temperature (Te) of stage I garnets (−38 to - 26 °C) is very close to the H_2O-$MgCl_2$ system (Supplementary Fig. S4). Te of stage II garnets varying from −32 to -19 °C might indicate a mixing between $MgCl_2$ and $NaCl_2$ systems. Te of epidotes from stage II plot in the mixing zone of the $MgCl_2$ and $NaCl_2$ systems. Te of quartz from stage II varies in a wide range (−46 to -9 °C) and coincides with the temperature range of $CaCl_2$-$MgCl_2$-$NaCl_2$ system. Tes of fluorites from stage II (−33 to −21 °C) indicate a mixture of $MgCl_2$-$NaCl_2$ (Supplementary Fig. S4). Results of Te indicate that the early stage of mineralization was dominated by $MgCl_2$-$NaCl_2$ whereas H_2O-$NaCl_2$ system governed the salinity of succeeding periods.

9. Stable isotope studies

9.1. Oxygen and carbon isotope composition of calcites

Results of carbon ($\delta^{13}C$) and oxygen ($\delta^{18}O$) isotope analyses of calcites collected from drill holes and carbonate host rocks, calcite from skarn zones, and carbonate veins are given in Table 3. $\delta^{18}O$ value of Keban Marble (25.43 ‰) is higher than those of manganiferous limestone (24.49 ‰) and limestone of the Nimri Formation (21.44 ‰), and ore-bearing carbonate veins (18.3 to 20.9 ‰) (Table 3). There is a sharp decrease in $\delta^{18}O$ values from limestone to calcites in the skarn zones. $\delta^{18}O$ of calcites from the Gr-Pyx-Plg skarn (18.24 ‰; stage I) is relatively high but gradually decreases to Ve-Gr skarn (15.13 ‰, stage I), Ve-Pyx-Gr skarn (12.96 ‰) and Gr skarn (12.83 ‰) of stage II (Fig. 12; Table 3).

$\delta^{13}C$ value of Ve-Pyx-Gr skarn (−4.63 ‰) of stage II is slightly lower than those of Gr skarn (−3.68 ‰; stage II), Ve-Gr skarn (−2.24 ‰; stage I) and Gr-Pyx-Plg skarn (−3.49 ‰; stage I) pointing to carbon of igneous origin (Fig. 12; Table 3). $\delta^{13}C$ value is 0.7 ‰ for Keban Marble, 2.09 ‰ for limestone of the Nimri Formation, 1.5 ‰ for manganiferous limestone, and 1.14 to 3.26 ‰ for ore-bearing carbonate veins (Table 3). $\delta^{13}C$ values of Keban marble, limestone and Mn-bearing limestone range from 0.7 to 2.09 ‰, which fall within the range of marine carbonates (Fig. 12).

9.2. Sulfur isotope composition of sulfides

Isotopic composition of sulfur is analyzed in galena, sphalerite, bornite, chalcopyrite, and pyrite collected from drill holes KS-17, KS-18, and KS-19. The results are given in Table 4 and frequency histograms are shown in Supplementary Fig. S5. $\delta^{34}S$ values of sulfides in drill hole KS-17 are from −8.5 to 1.8 ‰, those from drill hole KS-18 are −2.9 to −0.9 ‰ and $\delta^{34}S$ value of pyrite from KS-19 is −3.5 ‰. Regarding sulfur isotopic composition of sulfides, $\delta^{34}S$ is in the range of −4.6 to −1.0 ‰

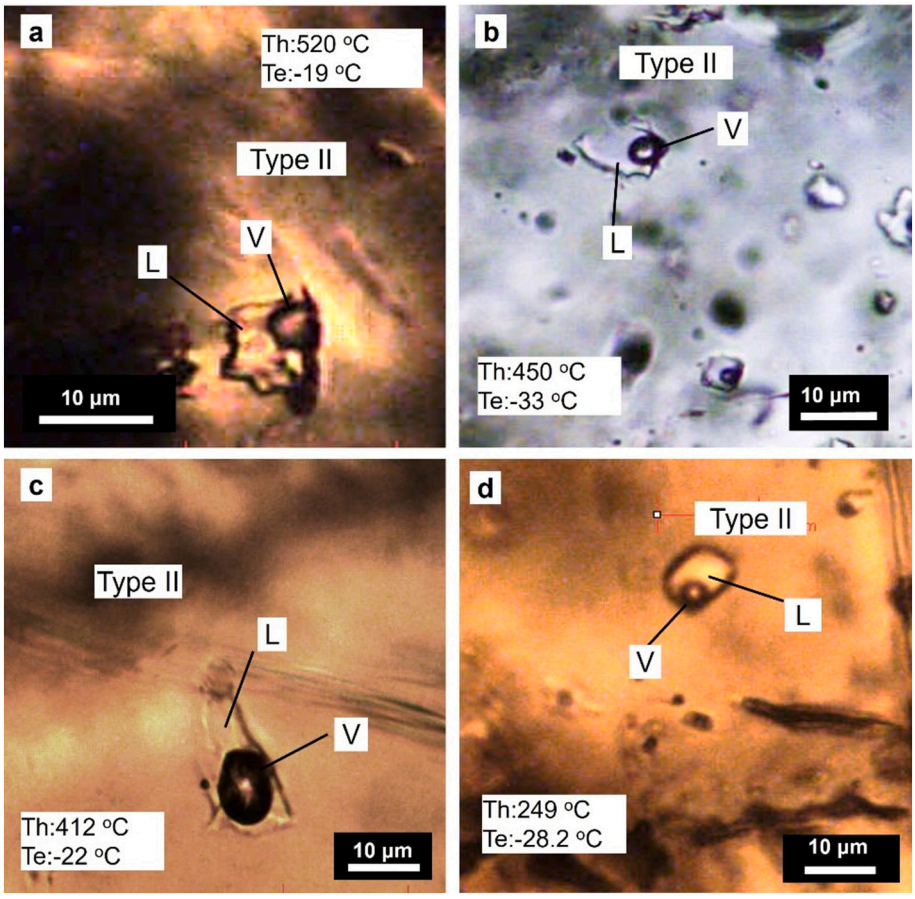

Fig. 10. Photomicrographs of primary FIs representing different stages of mineralization: liquid rich LV-type inclusion in garnet from stage II (a); LV-type inclusion in quartz from stage II (b); LV-type inclusions in fluorite (c) and calcite dfrom fluorite+pyrite+quartz+calcite vein. (V: gas phase, L: liquid phase, Th: homogenization temperature. Te: eutectic temperature).

for galena, from −8.5 to 0.6 ‰ for sphalerite, from −5.7 to 2.1 ‰ for pyrite, −0.9 to 1.8 ‰ for chalcopyrite and − 1.2 ‰ for bornite.

10. Discussion

10.1. Distribution of trace elements in sphalerite

It was shown that trace element characteristics of sulfide minerals are closely related to their crystallization temperature (Cook et al., 2009; Ye et al., 2011; Lockington et al., 2014; Frenzel et al., 2016; Bauer et al., 2019a; Xing et al., 2021). For instance, sphalerite from high-temperature hydrothermal base-metal deposits associated with magmatic-hydrothermal fluids tends to be more enriched in elements such as Fe, Mn, Co, and In (Cook et al., 2009; Ye et al., 2011; Lockington et al., 2014; Frenzel et al., 2016; Bauer et al., 2019a). However, some of elements in sphalerite such as Ga, Ge, As, Cd, and Tl are associated with low-temperature hydrothermal fluids (Kelley et al., 2004; Cook et al., 2009; Ye et al., 2011; Frenzel et al., 2016; Bauer et al., 2019a; Zhuang et al., 2019; Hu et al., 2021). In the Keban skarn deposit, sphalerites are represented by low to moderate Fe (av. 3.25 wt%), high Mn (av. 4819 ppm), Ga (av. 919 ppm), As (av. 516 ppm) and low Co (avg. 18 ppm) and In (av. 27 ppm) contents indicating that crystallization took place under low to moderate temperatures (Supplementary Table T6). The incorporation and fractionation of Fe in sphalerite are generally controlled by pressure and temperature conditions, pH, or sulfur fugacity of the fluid (Anderson, 1973; Frenzel et al., 2021). The variation in the Fe content strongly correlates with color differences of sphalerite in Keban, with dark-colored (dark brown) sphalerite-I having higher Fe contents relative to the light-colored (yellow-light brown) sphalerite-II. The variations in Fe between dark-colored and light-colored sphalerite can be interpreted as a result of decreases in temperature and/or increases in sulfur fugacity (e.g., Scott, 1983; Jiang et al., 2021). In addition, the inverse relation between Zn and Fe concentrations in sphalerites suggests relatively low temperatures for the ore-forming fluids (Wright and Gale, 2010).

The element distributions (e.g. Co, Mn, Ga, Ge, and In) in the skarn deposits are used for the petrogenetic assessment (Bauer et al., 2019a; Cook et al., 2009; Lockington et al., 2014; Ye et al., 2011). Systematic enrichment of Co in sphalerite is more common for skarn systems than VMS, SEDEX, MVT and epithermal deposits (Cook et al., 2009). High Co and Mn concentrations are very typical of skarn sphalerites (Ye et al., 2011). However, Co is a siderophile element and it may be selectively concentrated in pyrite relative to sphalerite (Lockington et al., 2014; George et al., 2016). Sphalerites in the Keban skarn deposit have low Co contents (Supplementary Table T6), which is most likely due to the preferential partitioning of Co into pyrite (e.g. Xing et al., 2021).

Mn concentrations of several hundred to a few thousand ppm are common in sphalerites (Cook et al., 2009). Skarn sphalerites are reported to have a narrow concentration range (with most values between 1000 and 6000 ppm; Cook et al., 2009; Ye et al., 2011). In the Keban deposit, Mn concentrations of sphalerites are similar to those from most skarn deposits (avg. 4819 ppm, Supplementary Table T6; Fig. 9).

Sphalerite is a significant host mineral for Ga (Cook et al., 2009; Bauer et al., 2019a). Gallium may be enriched in low-temperature carbonate-replacement deposits without a magmatic source. Low concentrations of Ga are also reported in skarn systems (Cook et al., 2009; Ye et al., 2011). The Keban sphalerites contain significant concentrations of Ga (Supplementary Table T6) which might suggest that crystallization

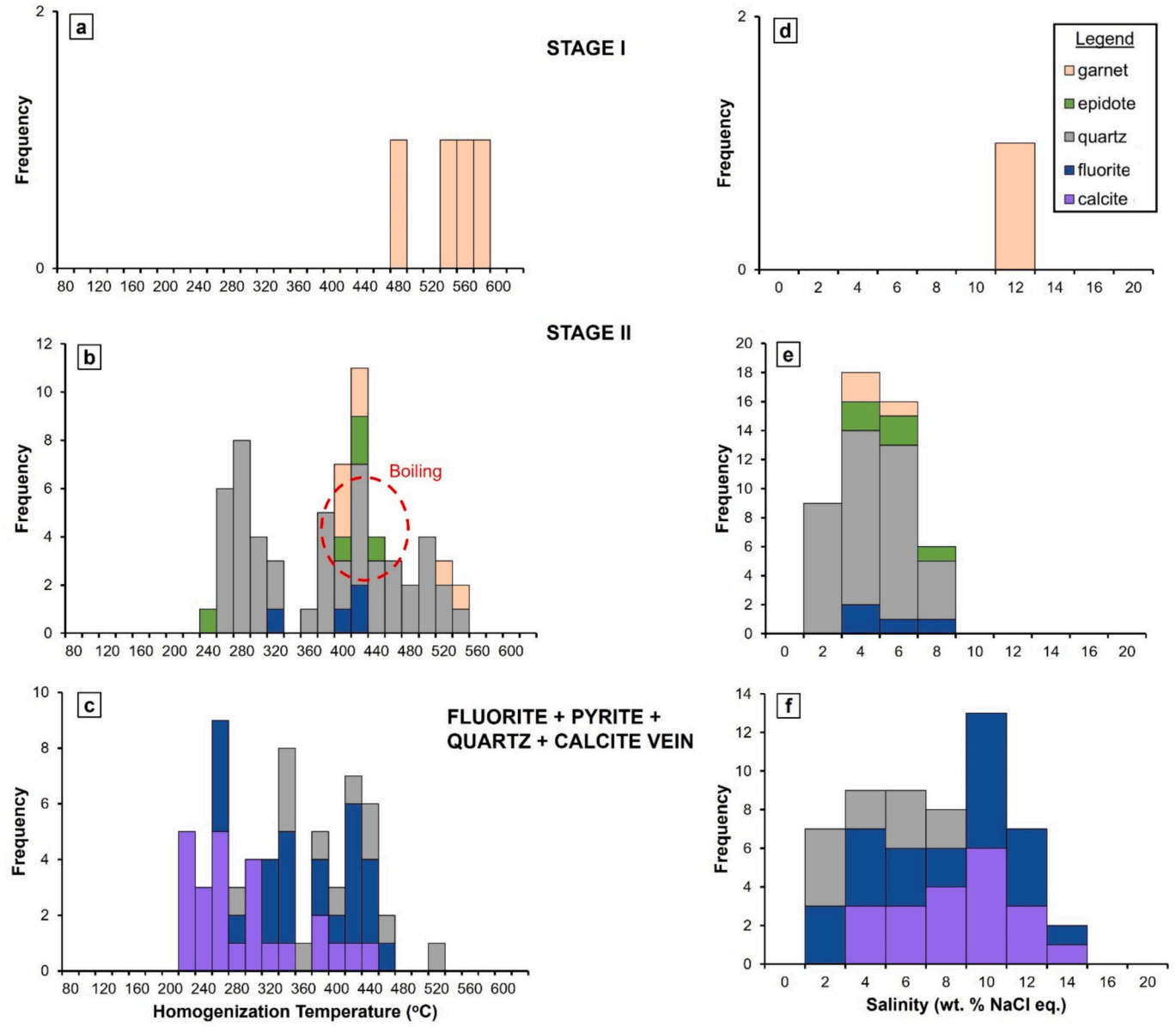

Fig. 11. Histograms of homogenization temperature and salinities for FIs in: (a, d) stage I; (b, e) stage II; (c, f) fluorite+pyrite+quartz+calcite vein from the Keban skarn deposit.

Table 3
Oxygen and carbon isotope composition of calcites from limestone and manganiferous limestone of Nimri Formation, ore-bearing carbonate veins, Keban marble and skarn zones.

Rock Type	Sample no.	Host rock/Mineral facies	Stage	Min. assemblage	$\delta^{13}C$	$\delta^{18}O$
					VPDB (‰)	VSMOW (‰)
Marble	B-KS2–9	Keban marble		Calcite	0.7	25.43
Limestone	KS-17-18	Nimri Fm limestone (60.40–63.40 m)		Calcite	2.09	21.44
	KS-17-28	Nimri Fm manganiferous limestone (131.00–134.10 m)		Calcite	1.51	24.49
Outer alteration zone	KS-17-45	Ore-bearing carbonate vein (386.3–387.5 m)		Sphalerite	3.26	20.9
	KS-17-55	Ore-bearing carbonate vein (592 m)		Sphalerite	1.14	18.26
Endoskarn	B-KS3–7	Gr-Pyx-Plg skarn	Stage I	Garnet, pyroxene	−3.49	18.24
Exoskarn	KS-17-53	Ve-Gr skarn (531 m)	Stage I	Garnet, vesuvianite, quartz, pyrite	−2.24	15.13
	D-KS2–1	Ve-Pyx-Gr skarn	Stage II	Garnet, vesuvianite, sericite	−4.63	12.96
	Sample1	Gr skarn	Stage II	Fluorite, phlogopite, muscovite	−3.68	12.83

took place at low-temperature conditions.

Indium concentrations in sphalerites from hydrothermal ore deposits and skarn systems range from <0.01 to 6.9 wt% (Bauer et al., 2019a, 2019b; Cook et al., 2009). Low In contents in skarn deposits may be due to 1) low crystallization temperature; 2) the distal character of skarn systems (Cook et al., 2009; Ye et al., 2011), and 3) the absence of Cu-

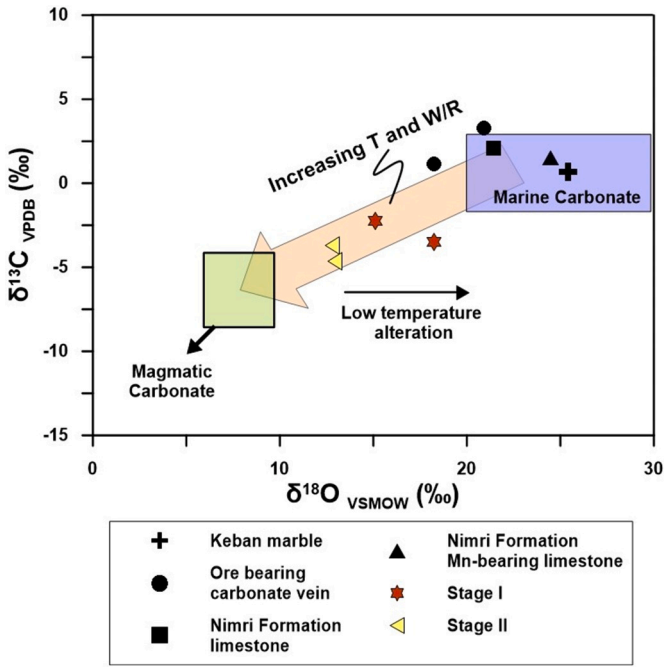

Fig. 12. Carbon-oxygen isotopic composition of the Keban skarn deposit. Carbon and oxygen isotope data of magmatic carbonate calcite and marine carbonates are from Bowman (1998) and Zheng (2001), respectively. The increasing temperature (T) and water/rock interactions (W/R) are indicated by the orange arrow (Ren et al., 2015).

Table 4
$\delta^{34}S$ values of sulfide minerals (CDT ‰).

Sample No	Mineral	Sample description	Depth (m)	$\delta^{34}S$
KS-17-43	galena	Galena, sphalerite and rare pyrite in 0.5 cm calcite vein	349.9–350	−1.0
KS-17-45	sphalerite	Abundant sphalerite with galena in the calcite vein	386.3–387.5	0.6
KS-17-47	chalcopyrite pyrite	massive pyrite formations, chalcopyrite, pyrrhotite	420–421	1,8 2.1
KS-17-55	sphalerite	sphalerite, chalcopyrite, and pyrite veins	592	−0.2
KS-17-56	pyrite galena	sphalerite vein, galena, pyrite, and abundant chalcopyrite	598	−2.9 −4.6
KS-17-58	pyrite sphalerite	5 cm pyrite-chalcopyrite vein, sphalerite, and disseminated galena	608–611	−5.7 −8.5
KS-17-60	pyrite	massive pyrite vein with a thickness of 0.5–5 cm	669	−4.5
KS-18-1	pyrite	chalcopyrite and pyrrhotite with massive pyrite vein	153.1	−2.8
KS-18-9	pyrite	2–5 cm pyrite vein in the limestone	399.9–400.3	−1.0
KS-18-10	pyrite	Massive pyrite-chalcopyrite-pyrrhotite vein with a thickness of 1.5–2 cm	406.3	−2.9
KS-18-13	pyrite	5 cm massive pyrite-chalcopyrite vein	453.4	−1.0
KS-18-18	pyrite	5 cm pyrite vein	523	−1.6
KS-18-20	chalcopyrite bornite	disseminated chalcopyrite in massive pyrite with fluorite, pinkish calcite and quartz	585.9–586.3	−0.9 −1.2
KS-18-22	pyrite	Pyrite clusters, disseminated sphalerite, and fluorite in a 3 cm quartz vein	666.3	0.8
KS-19-4	galena	0.2–0.3 cm stokwork galena	120.5–123.6	−3.5

bearing minerals coexisting with sphalerite (Bauer et al., 2019b). In the Keban deposit, low indium concentrations within sphalerites (Supplementary Table T6) might indicate deposition at low temperatures. Galena generally demonstrates a wide range of Ag, Sb, and Bi contents (e.g., Lueth et al., 2000; Hu et al., 2021). Galena samples at Keban are represented by high Ag (av. 4719 ppm) and Sb (av. 18,747 ppm) concentrations that are similar to those of magmatic-hydrothermal systems (i.e., skarn, VMS, and SEDEX; George et al., 2016). Pb, Sb, As, and Ag sulfosalts are also observed in galena and sphalerite, suggesting that these sulfosalts can be considered as pathfinder for Au (e.g., Yıldırım et al., 2019b).

10.2. Origin of hydrothermal fluids and metals

The overall oxidation state of a magma can be inferred from the differentiation of iron in a pluton, which in turn has significant implications for sulfur content and speciation, fluid separation, and total metal content of related skarns (Shimazaki, 1976; Newberry and Swanson, 1986; Simon et al., 2003). Cu, Zn, and Mo skarn plutons are more oxidized, while Au and Sn skarn plutons are more reduced compared to the average for all skarn-associated plutons (Meinert et al., 2005). Some assumptions regarding the melt behaviour and differentiations of the plutons associated with skarns can be made by monitoring the distribution of different trace elements. Sc, V and Ni, that are expected to decrease as crystallization and differentiation proceed, have high concentrations in plutons associated with calcic Fe skarns and decrease progressively through Au, Cu, Zn, and W skarns (Meinert et al., 2005). The high Rb/Sr ratios imply that the formation of W, Mo and Sn skarns is mostly dependent on the differentiation process rather than a specific magma composition (Newberry and Swanson, 1986). Contrarily, there is limited evidence of differentiation in the Fe, Au, and, to a lesser extent, Zn skarn systems; which can be atributetd to either distinct magma compositions or other petrologic processes. Keban Magmatics represented by high Rb concentration (138–276 ppm) and relatively high V (35–63 ppm) and low Ni (0.5–5.5 ppm) contents (Kırat, 2020) indicate that both differentiation and magma composition affect the skarn mineralization.

Porphyry Cu ± Mo ± Au deposits are frequently related to intermediate composition arc-related igneous rocks with high Sr/Y (and La/Yb) ratio and the primary factor contributing to the increased fertility of arc magmas is their high-water content, which is necessary for the formation of magmatic-hydrothermal ore deposits upon shallow crustal emplacement (Richards, 2011). The maximum metal levels in the subsequent aqueous phase require oxidized and water-rich (> ~ 4 % wt%) parental magmas (Burnham and Ohmoto, 1980; Candela and Holland, 1986; Candela and Piccoli, 2005; Richards, 2005). The aqueous phase becomes saturated in magmas with high water contents, allowing for the effective partitioning of ore metals; and high oxidation states block the precipitation of magmatic sulphides, such as pyrrhotite, which may retain metals before they can separate into the aqueous phase (Sillitoe, 2010). Water saturation in magmas associated with skarns is affected by volatiles other than water, such as CO_2 (Holloway, 1976), and CO_2 is more abundant than CH_4 in more oxidized systems such as Cu and Zn skarns (Megaw et al., 1988; Baker et al., 2004). In the Keban skarn deposit, almost all the first and late-stage FIs are CO_2-rich.

There are similarities between the fluid evolution of skarn deposits and some porphyry systems, and the bulk-metal budget is governed by the magmatic hydrothermal fluid in both deposit types (Baker et al., 2004; Hou et al., 2015; Zheng et al., 2015). Moreover, these deposits are represented by high temperature and high salinity fluids with abundant CO_2 (Baker and Lang, 2003; Meinert et al., 1997, 2003; Shu et al., 2013; Peng et al., 2015; Xu et al., 2016).

Particularly, garnet and pyroxene are good indicators for calc-silicate alteration crystallizing from the magmatic-hydrothermal fluids. FIs hosted in garnet in stage I yield high homogenization temperatures (473 to 572 °C) and relatively moderate salinities (11.9 wt% NaCl). As the

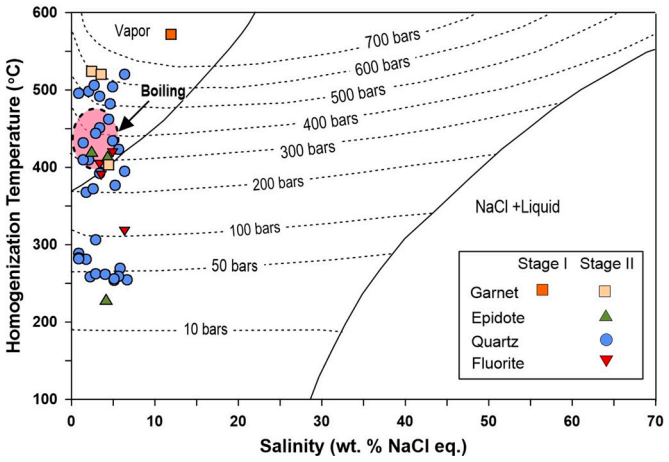

Fig. 13. Pressure estimates FIs of the Keban deposit from different stages. Isobars were calculated using the equations of Driesner and Heinrich (2007).

temperature decreases, salinity is lowered (Fig. 13). Formation of epidote and quartz has coincided with the decrease in temperature and salinity of fluid which represents the transition to stage II involving low to moderate temperature (230 to 520 °C) and low to moderate salinity (0.8–6.6 wt% NaCl eq.). Considering the order of formation of minerals, Th and salinity of garnet in stage I and epidote in stage II are consistent with those of quartz.

The early fluid compositions of many skarn systems are remarkable in that they have extremely high $CaCl_2$ ($\pm MgCl_2$) that results from the carbonate dissolution (Kwak and Tan, 1981; Kwak, 1986). Stage I at the Keban skarn deposit is characteristic of H_2O-$MgCl_2$ composition whereas stage II is represented by H_2O-$CaCl_2$-$MgCl_2$-$NaCl_2$. The change in composition of the FIs from $MgCl_2$ to $CaCl_2$-$MgCl_2$-$NaCl_2$ from stage I to II indicates that at the beginning of the skarnization, hydrothermal solutions interacted with dolomitic host rocks. During later stages, increasing interaction with carbonate host rocks might be resulted in a change leading to H_2O-NaCl-$CaCl_2$-dominated composition (Supplementary Fig. S4).

It is also possible that the fluid of the Keban skarn system contains KCl which is a common component in magmatic-hydrothermal systems as well as other solutes (Lecumberri-Sanchez et al., 2020). In hydrothermal deposits, volatiles like Cl and S can form complexes with a wide range of elements, including the alkaline and alkali-earth elements (K, Na, Ca) and the ore-forming elements (Cu, Au, Pb, Zn, Fe, Mo). These complexes are essential for the subsequent mineralization processes and the distribution of ore metals (Frank et al., 2003; Williams-Jones and Heinrich, 2005; Simon et al., 2006; Zajacz and Halter, 2009). For mineralization in porphyry and skarn deposits, which are primarily derived from the parental magma (Meinert et al., 2005; Sillitoe, 2010), volatile and ore element contents are generally considered to be advantageous (Halter et al., 2005; Stern et al., 2007; Chelle-Michou and Chiaradia, 2017).

Transport of Zn and Pb is strongly dependent on Cl content of the brine, liquid-rich inclusions and, to a lesser extent, vapor-rich inclusions (Baker et al., 2004). Cl complexes are shown to be effective agents in the transport of Pb and Zn in hydrothermal solutions at high temperatures (e.g., Frank et al., 2003; Baker et al., 2004; Williams-Jones and Heinrich, 2005; Simon et al., 2006; Zajacz and Halter, 2009). Although crush-leach analysis is not available for the studied FIs, $MgCl_2$-$NaCl_2$ dominated liquid-rich fluid inclusions with wide range of salinity in stage II might support that Pb, Zn and Cu are likely transported by Cl complexes.

Salinities of FIs from fluorite+pyrite+quartz+calcite vein (fluorite, quartz, and calcite) vary in a wide range from 0.3 to 12.2 wt%. NaCl and homogenization temperatures fall in the range of 212 to 503 °C (Table 2). Relatively moderate temperature and salinity values of primary LV-type FIs in stage II fluorites and quartzs (LV-type fluorite: 317–419 °C; 3.4–6.3 wt%, LV-type quartz: 254–520 °C; 0.8–6.6 wt%) indicate that the stage II minerals are influenced by the fluorite+pyrite+quartz+calcite vein. This vein is most likely associated with the Keban fluorite mineralization, a part of the metallogenic province. Öztürk et al. (2019) reported that the average homogenization temperatures and salinities of the fluorites in this deposit are >600 °C and 61 wt% NaCl for L + S + V inclusions and 312 °C and 17 wt% NaCl for L + V inclusions. The high salinity measured in FIs of calcite and quartz associated with these fluorites is not much of a surprise (Table 2). Low to medium temperature and salinities measured in the late-stage garnet and epidote are due to cooling and diluting effect of meteoric water (Fig. 13).

The isotopic analysis of calcite can provide information on the carbon and oxygen isotopic composition of the fluids during the later stages of skarn mineralization (Shimazaki et al., 1986). The primary sources of carbon in the ore-forming fluids are: a) magmatic or mantle-derived carbon with isotopic composition ranging from −9 to −3 ‰ or − 5 to −2 ‰, respectively (Taylor, 1986); b) carbon with an isotopic composition ranging from −10 to just above 0 ‰, either from dissolution of sedimentary carbonate or from the interaction of brine and mudstone (Rollinson, 1993), seawater carbon isotopic composition remaining near 0 ‰ (Veizer et al., 1980); c) organic materials represented by ^{12}C rich carbon with isotopic composition ranging from −30 to −15 ‰ (Ohmoto, 1972).

Carbon isotope compositions of carbonate host rock in the Keban deposit are consistent with the range suggested for the marine carbonates (−3 to +3 ‰) (Hoefs, 1987; Clark and Fritz, 1997). However, the degree of ^{13}C depletion observed in the Keban skarns and ore-bearing carbonate veins is highly consistent with simple decarbonation and dissolution of the marine carbonates (Fig. 12). The $\delta^{13}C$ of Stage I and II calcites (−4.49 to −2.24 ‰) from the Keban skarns shows an igneous-derived carbon isotope signature, indicating a magmatic fluid source. However, since the $\delta^{13}C$ value (−4.63 to −3.68 ‰) is slightly depleted, calcic skarn shows a signature of low-temperature alteration (e.g. Barnes, 1979, 1997).

The $\delta^{18}O$ values of calcites from the skarn zones range between 12.83 and 18.24 ‰, which are greatly higher than the meteoric water composition most probably due to isotopic exchange with fluids from adjacent carbonate wall rocks (e.g. Nabatian et al., 2017). Oxygen isotope values of ore-bearing carbonate veins (18.2 to 20.9 ‰) are generally consistent with average limestone values varying between 17 and 31 ‰ (Rollinson, 1993). It is evident that any hydrothermal fluid with low $\delta^{13}C$ and $\delta^{18}O$ values might have occasionally interacted with the limestone to cause the observed trend of carbon and oxygen isotope values (Fig. 12).

Volatilization, fluid infiltration, and the degree of fluid-rock interaction are the major mechanisms responsible for the depletion of $\delta^{13}C$ and $\delta^{18}O$ in calcite (Bowman et al., 1985; Valley, 1986; Holness, 1997; Shin and Lee, 2003; Orhan et al., 2011). Fluid–rock interaction led to isotopic depletion of Keban skarn calcites through calc-silicate producing processes and permeability increase driven by substantial infiltration of meteoric water into the system, which is also supported by the results of fluid inclusion studies (e.g., Orhan et al., 2011, Demir and Dişli, 2020). The salinity of 11.9 wt% NaCl eq. in the stage I decrease to 0.8.-6.6 wt% NaCl eq. in the stage II (Table 2). Likewise, the heavy isotopes of carbon and oxygen in the rock are depleted as a result of isotopic exchange between CO_2 and carbonate rocks at high temperatures (Bowman, 1998).

Sulfur isotope values of sulfide minerals in hydrothermal ore deposits have been the subject of various studies (e.g., Rye and Ohmoto, 1974; Ohmoto and Rye, 1979; Ohmoto and Goldhaber, 1997). According to Ohmoto and Rye (1979) and Hoefs (1987), sulfide minerals forming in the skarn deposits have an average $\delta^{34}S$ of 1.75 ‰. $\delta^{34}S$ values of major earth reservoirs are as follows: −20 to +20 ‰ for metamorphic rocks, +22 ‰ for marine sulfates, and 0 to +10 ‰ for

granitic rocks (Hoefs, 1987). The sulfur in mineral deposits may be derived from multiple sources: organic reduction of seawater (<−10 ‰), magmatic (0 ‰), and marine sulfur (>10 ‰) (Rollinson, 1993). The $\delta^{34}S$ histogram prepared for the Keban deposit displays a normal distribution, with all samples plotting within a relatively wide range (−8.5 to +2.1 ‰), indicating that S in the fluid was transported as HS^- and S^{2-} and derived from a magmatic source, given the relatively low oxygen fugacity during the retrograde-sulfide stage (stages II) (Supplementary Fig. S5) (e.g., Li et al., 2020). $\delta^{34}S$ of studied sulfides is similar to those of pyrites from the Keban Pb—Zn deposits (−0.5 to 0.1 ‰: Kalender, 2011), Kalkım-Biga peninsula Pb-Zn-(Cu) deposit (−1.2 to 1.5 ‰: Akıska et al., 2013), skarn deposits from the Qimantagh metallogenic belt (−2.2 to 4.1 ‰: Zhong et al., 2018), Beiya polymetallic Au deposit (−4.1 to 0.6 ‰: He et al., 2017), Balugou Cu-Pb-Zn skarn deposit (−2.1 to 0.9 ‰: Ding et al., 2016) and Arqiale skarn Pb—Zn deposit (−7.1 to 2.6 ‰: Dai et al., 2019), and their S isotopic compositions indicate a homogeneous magmatic source (−3 ‰ to +1 ‰, Hoefs, 2009) (Supplementary Fig. S6).

10.3. Fluid evolution and mineral precipitation

Fluid inclusions described in the Keban skarn deposit provided evidence for a sequence of events with variable amounts of separation, boiling, and mixing (or dilution). In stage I, garnet ($Adr_{3.22–94.62}$ $Grs_{2.39–90.04}$ $Prs_{3.57–20.51}$) is a major anhydrous prograde skarn mineral accompanied by trace amount of diopside-rich pyroxene (Fig. 7a-c). The high homogenization temperature (473 to 572 °C) and moderate salinities (11.9 wt% NaCl) of the FIs measured in the studied garnets are comparable to the temperatures of typical prograde skarn assemblages (~400–650 °C) (Einaudi et al., 1981; Shu et al., 2013; Peng et al., 2015; Xu et al., 2016). The prograde assemblage crystallization temperature is also verified by the temperature of 480–558 °C calculated by the garnet-pyroxene thermometry for the stage I (Supplementary Table T7) (Ravna, 2000). During this stage, fluids separated straight from silicate melts at elevated temperatures (~570 °C). No obvious boiling and fluid mixing occurred. Consequently, LV-type hypersaline brines (Figs. 13 and 14) are discovered as trapped within the garnet. Microthermometric studies of the Keban skarn deposit have demonstrated that the solutions during the early skarn stage have a H_2O–NaCl–($\pm MgCl_2$) composition (Table 2, Supplementary Fig. S4) (Roedder, 1984; Shepherd et al., 1985).

Subsequently, a shift proceeded from the closed system of Stage I (lithostatic conditions) to the open system of Stage II (hydrostatic conditions). With the steady addition of meteoric water, the temperatures and salinites of the ore-forming hydrothermal fluid decreased to 230–524 °C and 0.8–6.6 wt% NaCl equiv., respectively (Table 2). This, in turn, resulted in the precipitation of significant amount of sulfide phases (e.g. Drummond and Ohmoto, 1985). The composition of solutions trapped in the retrograde stage (e.g. low-moderate temperatures) is H_2O–NaCl–($\pm CaCl_2$ ± $MgCl_2$) (Table 2, Supplementary Fig. S4) (Roedder, 1984; Shepherd et al., 1985).

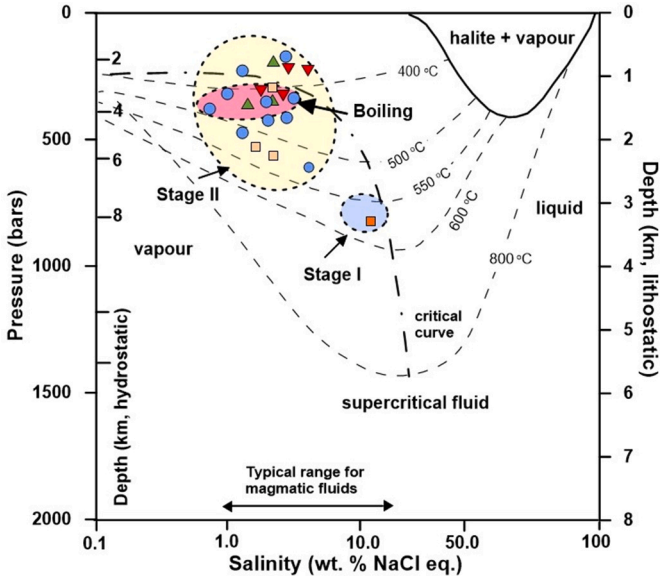

Fig. 14. Pressure-salinity diagram showing the phase relations in the NaCl-H_2O system (modified from Wilkinson, 2001 after Fournier, 1987 and Bodnar, 1995). Symbols are the same as Fig. 13.

The temperatures of 200 to 485 °C calculated by the garnet-pyroxene thermometry for the stage II at 500 bar are agreement with the homogenization temperatures of stage II (Supplementary Table T7) (Ravna, 2000). This shift resulted in the mixing of the early, hot, hypersaline brines with meteoric water, boiling of the fluids, and subsequent sulphide deposition. Therefore, FIs of LV-and VL-typeswith varying salinities become trapped in quartz, fluorite and calcite (Figs. 13 and 14). Additionally, it is believed that the extent of mixing with meteoric water was significant since the salinities are well correlated with the homogenization temperatures from the stage I to stage II (Figs. 13 and 14).

During stage II, the retrograde skarn minerals (e.g. epidote, muscovite, phlogopite, actinolite, calcite, and chlorite) overprinted the previous skarn assemblages in the alkali syenite porphyry by replacing the early garnet (Fig. 5g, h), pyroxene and altering feldspar and other mafic minerals. In this stage, galena, sphalerite, chalcopyrite, and pyrite predominantly occurred within the calcite, quartz, and fluorite veins.

Fluid boiling could have occurred in stage II at 395–496 °C and followed by the sulfide mineralization (e.g. Chen et al., 2017). It is likely that the sudden pressure drops and the release of CO_2 by boiling increased the permeability and triggered fracture formation at shallow depths (Kwak, 1986). After the boiling, sulfide minerals precipitated from the hydrothermal solutions that are partly contributed by meteoric fluids along the N-S trending fractures.

CO_2 is generated by decarbonization process that take places between carbonate rock and magmatic-hydrothermal fluids, which might originate through the exsolution from a deep magma body (Sisson and Hollister, 1990; Shinohara and Hedenquist, 1997). Regarding the Stage I at Keban, it was unlikely that the volatile exsolution from the plutonic complex was the ultimate source of CO_2 in the early fluids. Prograde decarbonization has been shown to be another mechanism to produce CO_2 through the interaction between high-temperature fluids and carbonate host rock (Sisson and Hollister, 1990). $\delta^{13}C$ values (−4.63 to −3.49 ‰) of calcites from the Stage II were strongly depleted in reference to those of Nimri limestone (1.51 to 2.09 ‰) probably indicating that CO_2 has been derived from a carbonate rock (Fig. 12). Consistent with the microthermometric data, the calcite $\delta^{13}C$ and $\delta^{18}O$ values from the Stage II were depleted by low-temperature and meteoric fluids.

Boiling is an efficient process for mineral precipitation (Drummond and Ohmoto, 1985; Heinrich, 2007; Wilkinson, 2001), and in a boiling fluid system, the FI trapping pressure is assumed equal to the external pressure (Roedder and Bodnar, 1980; Qi and Liu, 2002; Shu et al., 2013, 2021). Therefore, fluid boiling assemblages could be used to acquire exact estimates of trapping pressure from the microscopic temperature measurements of FIs (Roedder, 1984; Brown and Hagemann, 1995; Bouzari and Clark, 2006).

Regarding the boiling process in stage II, the trapping pressure can be estimated applying the correlation proposed by Driesner and Heinrich (2007) using the homogenization temperature and salinity values on a NaCl–H_2O P–T–X diagram. Accordingly, mineralization at stage II of the Keban skarn deposit was formed under hydrostatic pressure and depth conditions of ~100–500 bar and < 1.5 km, respectively (Driesner and Heinrich, 2007) (Figs. 13 and 14).

At the last stage (III), due to intense meteoric water influx, some of the minerals have undergone alteration; magnetite transformed to hematite and goethite, and pyrite, marcasite and chalcopyrite altered to limonite, chalcocite and covellite, respectively.

Detailed petrography and EPMA data demonstrated that the garnet composition changed from grossular (Grt 1) (Adr $_{17.77–23.76}$ Grs $_{63·29–67.90}$) to Fe-rich grossular (Grt 2) (Adr $_{34.06–50.88}$ Grs$_{29.62–50.48}$), to andradite (Grt 3) (Adr $_{53.44–94.62}$ Grs$_{2.39–16.05}$), and to grossular (Grt 4), (Adr $_{0.68–15.58}$ Grs$_{70.50}$) (Fig. 5c-e, i) indicating that the redox state of the ore-forming fluids changed from reduced to oxidized and then to reduced during the fluid evolution, as Fe^{3+} is incorporated into andradite in an oxidized environment and Fe^{2+} is hold in grossular under a reducing environment (Einaudi et al., 1981; Meinert, 1997; Misra, 2000) (Fig. 15b).

10.4. Mineral paragenesis and constraints on the evolution of hydrothermal fluids

Textural characteristics and mineral compositions of skarn zones show some differences, particularly in the endoskarn zone. Garnets of the endoskarn that occur as medium to coarse-grained euhedral isotropic grains with strong oscillatory zoning are of andradite-grossular (And$_{33.36–94.62}$ Grs$_{2.39–52.73}$) composition (Fig. 5c-e, g, h, 7b). Endoskarn pyroxenes recognized as dark green subhedral crystals show diopside composition (Hed$_{2.6–15.9}$ Dio$_{70.2–90.7}$ Joh$_{0.3–2.6}$) (Fig. 5f, 7c) and exoskarn pyroxenes are in the range of diopside-hedenbergite composition (Fig. 7c). Garnets of the exoskarn are small to medium-grained with weak oscillatory zoning and are of mainly grossular composition (And$_{33.36–90.44}$ Grs$_{64.87–90.44}$) and they have relatively high Ti contents (Fig. 5j, 7b). According to Einaudi and Burt (1982), the chemical compositions of pyroxenes and garnets are closely related to the skarn type. The increase in hedenbergite and johannsenite abundances and the decrease in diopside content of pyroxenes indicate a transition from Cu to Fe, W, and Zn—Pb type skarn deposits. Such a compositional shift in skarns is also possible by an increase in grossular and spessartine-+almandine abundances and a decrease in andradite content of garnets (Einaudi and Burt, 1982). Mn/Fe ratios of pyroxenes were found <0.1 for Cu—Fe type skarns, 0.1–0.2 for W type skarns, and > 0.2 for Pb—Zn type deposits (Nakano et al., 1994; Nakano, 1998). Mn/Fe ratios of pyroxenes in the Keban field are in the range of 0.001 to 0.17 indicating that studied skarn is of Cu and W-type deposit.

There has been a debate on the occurrence of chalcopyrite disease texture in sphalerite. The mineral assemblage yields that temperature of hydrothermal fluid decreased over time, causing the co-transportation of Cu and Zn in solution from which chalcopyrite and sphalerite eventually co-precipitated at temperatures close to 300 °C (Barton and Bethke, 1987; Brueckner et al., 2016). Both sulfide minerals are locally epitaxially intergrown and form chalcopyrite disease (Large, 1992; Ohmoto, 1996). In sphalerite, Fe frequently substitutes for Zn (Barton and Toulmin, 1966; Cook et al., 2009; Brueckner et al., 2016), which depends on the redox state of the coexisting hydrothermal fluid (Barton and Toulmin, 1966). In contrast, the diffusion-controlled replacement of Fe by Cu in Fe-rich sphalerites, and chalcopyrite-sphalerite co-precipitation are the most likely mechanisms for the development of replacement texture, so called chalcopyrite disease in sphalerite (Nagase and Kojima, 1997; Govindarao et al., 2018 and references therein).

Textural characteristics and mineral chemistry indicate that sphalerite-I probably formed under reducing conditions with Fe content

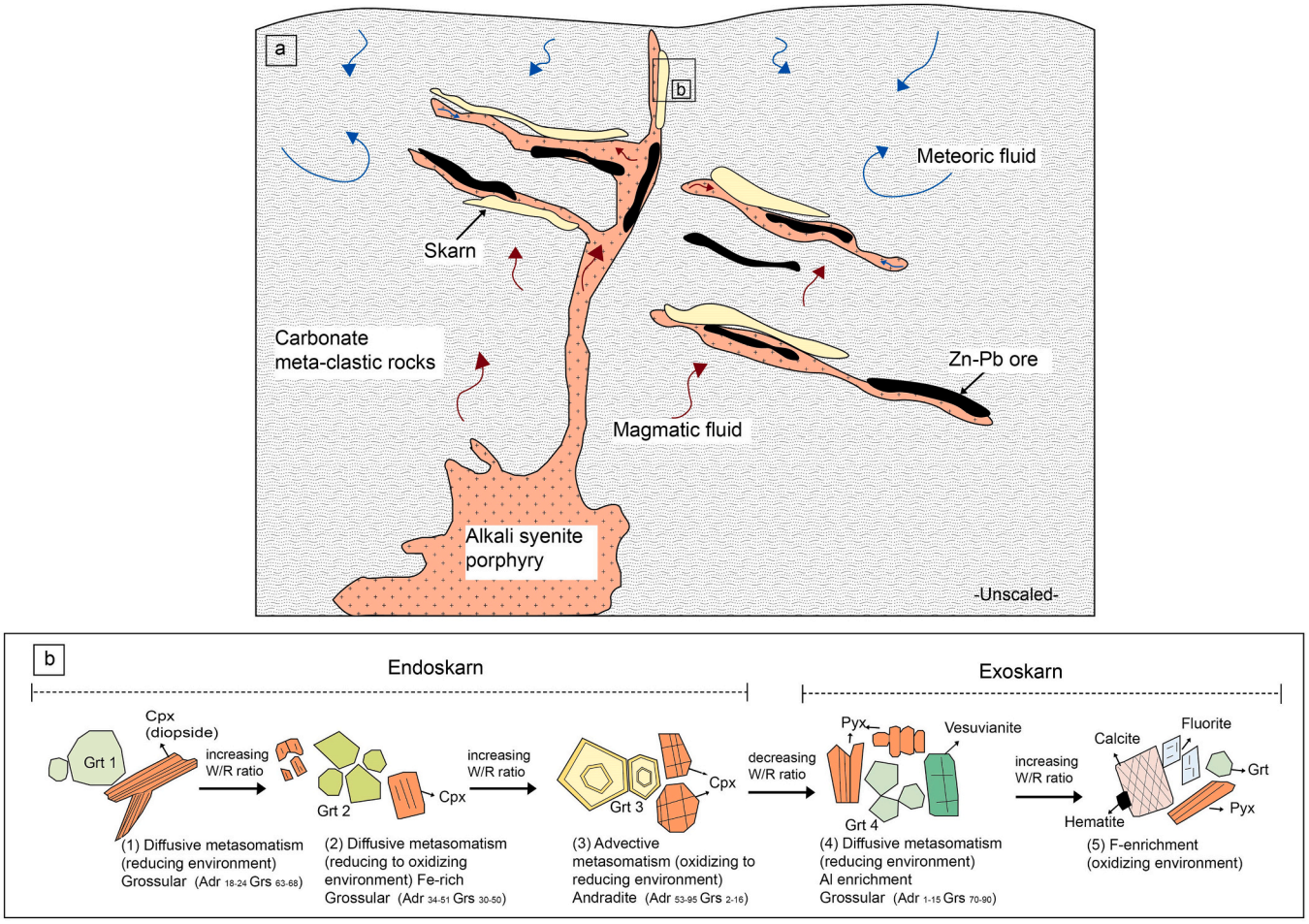

Fig. 15. a. Schematic diagram of fluid evolution and skarn formation process in the Keban deposit b. Conceptional model for the growth of Grt 1 to 4 and skarn minerals (Cpx: clinopyroxene; Pyx: pyroxene, Grt: garnet).

higher than sphalerite-II (Fig. 6a, d) (e.g., Raza et al., 2020). It is important to note that the sphalerite-I includes pyrite inclusions and chalcopyrite with replacement texture and is accompanied by magnetite-I while sphalerite-II is intergrown with galena-I and has chalcopyrite-II exsolutions with sulfosalt grains. Given these observations, the gradual decrease in temperature from dark sphalerite-I to late light-colored sphalerite-II was interpreted as evidence for progressive cooling of ore-forming fluid. After formation of sphalerite-I, slightly reduced hydrothermal fluids resulted in precipitation of Fe poor-sphalerite-II, galena-I, pyrite-I, and magnetite-I. Subsequently, chalcopyrite-II precipitation started to diminish with decreasing temperature. Sphalerite-III, pyrite I, II and III, magnetite-II, chalcopyrite-III and fluorite formed at the shallow subsurface environment (Supplementary Fig. S7). Hematite, secondary Cu minerals as covellite, and chalcocite formed in the supergene zone, which corresponds to the last phase of Zn–Pb–Cu mineralization at Keban.

According to previous studies on skarn systems, early garnets tend to be Al-rich whilst the latter ones favor Fe enrichment (e.g., Einaudi et al., 1981; Meinert, 1992, 1997; Park et al., 2017). At the Keban deposit, we note that late hydrothermal garnet is grossular-rich, which is also typical of various deposits (Tian et al., 2019; Ghosh and Upadhyay, 2022). It has been reported that the majority of these deposits have high F-fugacity and are related to Al-rich mineral phases that are transported as fluoride complexes (e.g., Ragnarsdóttir and Walther, 1985; Walther, 1997). As indicated by the presence of hydraulic breccias, hydro-fracturing triggers boiling and results in a continuous circulation of hydrothermal fluids (Peng et al., 2015; Wang et al., 2017; Tian et al., 2019). Sudden pressure changes due to the fracturing of hydrothermal system to the surface and possible contribution from meteoric waters in near-surface environments could cause the boiling of fluids in the Keban skarn system. This change induced by boiling, as well as the release of CO_2 and other gases, increased permeability and fracture formation towards shallow depths (Kwak and Tan, 1981; Kwak, 1986). The dominance of hydrous minerals including chlorite, epidote, tremolite, and allanite along the skarn zone can most likely be attributed to the injection of meteoric water. The boiling probably increases oxygen fugasity (fO_2) and Fe^{3+} activity (compared to Al^{3+}) in the residual fluid and contributes to the development of Fe-rich garnet zones. The original hydrothermal system is reactivated as the cracks are filled by hydrothermal fluids. The formation of Al-rich garnet zones is triggered by comparatively low fO_2 and high Al^{3+} activity (compared to Fe^{3+}) (e.g., Tian et al., 2019). Due to the absence of fluorite in Grt 4 and lack of evidence of boiling and hydraulic breccias, it is most likely that Grt 4 Al-rich garnets and vesuvianite were formed from residual metasomatic fluids that extract Al from the wall rocks, such as the calc-schist (e.g., Peng et al., 2015; Strmić et al., 2018). Brecciation of the host calc-silicate rocks and hydrothermal fluid infiltration are frequently witnessed in skarn deposits (Einaudi et al., 1981; Meinert, 1992). The fluid infiltration causes a number of decarbonization processes that improve the porosity of the rock and allow further fluid-rock interaction. Skarn systems in the Keban deposit chiefly evolved from diffusive metasomatism driven at a low fluid/rock ratio to more advective/infiltration-driven metasomatism at a higher fluid/rock ratio (Meinert et al., 2005).

We propose a conceptual model for the Pb—Zn mineralization and growth of Grt 1 to 4 at Keban (Fig. 15a, b). Under reduced conditions, magmatic-hydrothermal fluids initially separated from the alkali syenite porphyry and then interacted with the carbonate meta-clastics and precipitated grossular (Grt 1) rather than andradite under low water/rock (W/R) ratio. Due to the long pore fluid residence time in the closed systems, REE content of fluids generated by diffusive metasomatism is derived from magmatic-hydrothermal fluids and buffered by the composition of the host rocks (Liu et al., 2021). Following the deposition of grossular (Grt 1) in the endoskarn of Keban deposit, extensive infiltration occurred which resulted in the crystallization of Fe-rich grossular (Grt 2) with strong oscillatory zoning followed by the precipitation of andradite-dominated garnet (Grt 3) with high Fe^{3+} concentration at high W/R ratios.

Lessing and Standish (1973) suggest that hydrothermal systems with sharp contacts and narrow zones reveal rapid crystal growth and/or rapid compositional changes. Oscillatory zoning in these dynamic hydrothermal systems refers to a feedback between the mineral and the environment (fluid/melt) (Halden, 1996), in which changes in P, T, X along with surface adsorption, element diffusion, and growth rate can affect the development of zonation. The existence of oscillatory zoning suggests that garnets were formed during the infiltration metasomatism under disequilibrium conditions represented by a high fluid/rock ratio (Gaspar et al., 2008). Grt 2 cores and rims show sharp composition changes in Al, Fe^{2+}, Fe^{3+} and different optical features suggesting that the core and rims of garnets were originated from distinct fluid pulses. Their compositional relations imply that Grt 2 and Grt 3 in the endoskarn zone occurred at acidic conditions with high W/R ratio (Fig. 15b).

When the water-rock reaction diminished, infiltration of hydrothermal fluid caused the retrograde alteration of the calc-silicate assemblage producing hydrothermal garnet, vesuvianite, epidote, chlorite, muscovite, and phlogopite accompanied by magnetite and sulfides. The Grt 4 (grossular) and vesuvianite were mostly affected by Al-bearing residual metasomatic fluids that originated from calc-schist under reducing conditions. Pyroxene was crystallized in a disequilibrium system through the infiltrative metasomatism between magmatic fluids and carbonate meta-clastics. Following the precipitation of Grt 4, the system progressively changed to oxidized conditions with a low W/R ratio. The presence of calcic exoskarns with high amounts of hematite and fluorite suggests that the late skarn stage was deposited from F-rich oxidized fluids (Fig. 15b). The decreasing temperature and mixing with meteoric water led to the deposition of Cu, Pb, and Zn as sulfides. The ongoing mixing of fluids with large volume of cold meteoric water would decrease the temperature and increase the pH (neutralizing), thus promoting the supergene alteration.

10.5. Comparison with other distal Zn-Pb-(cu) skarn systems

The Keban Zn-Pb-(—Cu) mineralization contains several similar features with typical distal Zn skarn deposits (Einaudi et al., 1981; Einaudi and Burt, 1982; Meinert, 1992; Meinert et al., 2005):

(1) Related igneous rocks emplaced as shallow dike and sills (Meinert et al., 2005).
(2) Although the depth of skarn formation at Keban is not available in the literature, Keban deposit has no evidence of zoning (e.g., Ault and Williams-Jones, 2004) and shows similarities to shallow skarns (Zn- and Pb-rich) that have been reported to have shallow depth ($P < 1$ kbar, 200 Mpa) and low pressure (Shimizu and Shimazaki, 1981).
(3) Keban deposit has generated an apparent prograde skarn and retrograde alteration mineral assemblages which include garnet, clinopyroxene (mostly diopside), actinolite, chlorite, epidote, and tremolite (Einaudi and Burt, 1982; Yang et al., 2013; Xu et al., 2019). The clinopyroxene/garnet ratio of Keban deposit increases from endoskarn to exoskarn (e.g., Akıska, 2020; Xu et al., 2019).
(4) Chemical compositions of Keban garnets are broadly typical of Zn skarns (Einaudi et al., 1981; Meinert, 1983, 1992). Although commonly recognized in Pb—Zn skarn deposits (Meinert, 1987, 1992; Meinert et al., 2005), Keban pyroxenes with low Mn content most likely experienced diffusive metasomatism (e.g., Wang et al., 2023).
(5) The ore metals are dominated by Zn with abundant Pb, Fe, Cu, Ag, and Hg (e.g., Xu et al., 2019) (Supplementary Table T6).
(6) Magmatic fluids at Keban dominate stage I (prograde) and followed by stage II (retrograde+sulfides) dominated by shallower fluids of meteoric origin, resembling the ore fluids of typical skarn deposits (Shimazaki et al., 1986; Shimazaki, 1988; Megaw,

1998; Baker and Lang, 2003; Meinert et al., 2005). FI studies on the Keban deposit indicate that both the temperature and salinity slightly dropped from stage I (473 to 572 °C; 11.9 wt%) to stage II (230 to 524 °C; 0.8–6.6 wt%). However, especially stage II LV-type inclusions (e.g., fluorite and quartz) with relatively moderate salinities and moderate temperatures support the effect of subsequent magmatic fluids at are associated with the fluorite mineralization in the area.

(7) Homogenization temperatures recorded in ore-stage inclusions at Keban (230–524 °C) are similar to many other distal Zn skarn deposits, such as Trepča (350–475 °C: Strmić Palinkaš et al., 2013), Jinchanghe (117–550 °C: Huang, 2014), Hetaoping (109–498 °C: Yang et al., 2013; Chen et al., 2017), and El Mochito (~325–425 °C: Samson et al., 2008), and significantly higher than those of Luziyuan (110–316 °C: Xu et al., 2019).

(8) All Keban skarn calcites are significantly ^{18}O-depleted relative to protoliths like some other Zn—Pb and Zn—Cu (—Fe) skarn deposits (e.g., Shimazaki et al., 1986; Xu et al., 2019; Meinert et al., 2005; Orhan et al., 2011). For instance, a considerable $\delta^{18}O$ drop (up to +18 ‰) is reported in the distal Zn-(Pb—Ag) skarn deposit at El Mochito, Honduras resulting from O-isotope exchange between the ore fluids and limestone during W/R interactions (Vázquez et al., 1998).

(9) $\delta^{34}S$ values of the Keban sulfides (−8.5 to +2.1 ‰) are similar to those of Boashan distal carbonate-hosted Cu–Pb–Zn sulfides (−1.1 to +4.4 ‰; Ding et al., 2022) and Molchito distal Zn-Pb-Ag skarn deposit (−3.5 to +5.6 ‰; Ault and Williams-Jones, 2004) and, slightly lower than Luziyuan Zn-Pb-Fe(—Cu) distal skarn deposit (+8.9 to +12.0 ‰) which is originated from both magmatic and seawater sulfides (Xu et al., 2019). The sulfur isotope composition of the Keban deposit falls within the range of −8 to +5 ‰ that is reported for other Zn skarn deposits reflecting a magmatic source for sulfur (−3 to +3 ‰; Ohmoto and Rye, 1979). REE patterns of the Keban Magmatics, limestone, calcschist, marble, and skarn zones also imply that not only magmatic fluids but also solutions released from metamorphic host rock contributed to the formation of Keban Pb—Zn skarn deposit (e.g. Kalender, 2000, 2011; Kırat, 2020).

(10) The effect of meteoric water on the ore deposition at distal Zn skarn deposits is discussed by several studies (Einaudi et al., 1981; Bowman, 1998; Bodnar et al., 2014) which include Darwin-California, US (Newberry, 1987; Rye et al., 1974), Luziyan-Yunnan, SW China (Xu et al., 2019), Trepča-Priština, Kosovo (Strmić Palinkaš et al., 2013), El Mochito-Honduras (Vázquez et al., 1998; Williams-Jones et al., 2010) and Hetaoping and Jinchanghe, N Baoshan Block (Chen et al., 2017; Gao et al., 2011; Huang, 2014; Xue et al., 2008; Yang et al., 2013). On the contrary, boiling at 395–496 °C, temperatures and salinities of stage II inclusions, and $\delta^{34}S$ values of sulfides indicate that Keban mineralization was precipitated from a mineralizing fluid predominantly of magmatic origin.

11. Conclusions

The intrusion of the Late Cretaceous alkaline syenite porphyries into the Late Triassic carbonate rocks at Keban, southeast Turkey, formed a contact metamorphic zone and skarn type mineralization. The magmatic rocks form dyke swarms and skarnization occurs as irregular veins attaining a width of 15–20 m.

The mineralization at the Keban deposit involved a multistage paragenesis consisting of prograde (stage I), retrograde-sulfides (stage II), and supergene (stage III). Stage I garnets are andradite-grossular and the composition changes to grossular in stage II. Pyroxenes of stage I are represented by diopside and those of stage II are diopside-hedenbergite. Such compositional trends of garnets accompanied by Mn-poor pyroxene contents point to the existence of Cu skarn in the Keban area.

Garnets at Keban can be divided into grossular (Grt 1), Fe-rich grossular (Grt 2) and andradite (Grt 3) in the endoskarn zone and grossular-rich (Grt 4) in the exoskarn zone. This indicates that the redox state of the metasomatic fluids changed from reduced (with low W/R ratio) to oxidized conditions (with high W/R ratio) and then reduced conditions due to increasing interaction with the wall rock.

Mineral chemistry analysis on sulfides yielded that sphalerites with high Fe, Mn, and Ga contents were crystallized at low-moderate temperatures. Trace element concentrations of sphalerites suggest that mineralization was formed at distal part of the skarn system.

The homogenization temperatures measured on skarn minerals imply that fluid boiling developed during the retrograde stage and followed by sulfide mineralization. Stage II prevailed at a shallower environment (<1.5 km) and in pressures between ~100 to 500 bar which was also confirmed by low-temperature and low-salinity inclusions.

Carbon and oxygen isotope analyses on host rocks (marble and limestone), skarn zones, and vein calcites showed that heavy isotopes (^{18}O and ^{13}C) were depleted with increasing temperature, which is attributed to mixing between magmatic-hydrothermal fluid and meteoric water. $\delta^{34}S$ values of sulfide minerals indicate that magmatic fluids derived from the Keban Magmatics are likely to be the source of sulfur and metals forming the Keban skarn deposit.

Regarding spatial relations among the host rock, alteration zone, and mineralization, the Keban Pb—Zn deposit is quite similar to other Pb—Zn skarn systems. However, available data indicate that the Keban mineralization was affected by a nearby porphyry copper deposit and there could be a Pb-Zn-Cu skarn mineralization at the distal zone of this deposit.

CRediT authorship contribution statement

Ece Kırat: Writing – original draft, Visualization, Validation, Investigation. **Halim Mutlu:** Writing – review & editing, Supervision, Methodology, Funding acquisition.

Funding

This study was supported by the Ankara University [under grant number 18 L0443002].

Declaration of competing interest

The authors declare the following financial interests/personal relationships which may be considered as potential competing interests: ECE KIRAT reports financial support was provided by Ankara University. If there are other authors, they declare that they have no known competing financial interests or personal relationships that could have appeared to influence the work reported in this paper.

Acknowledgments

The Ankara University is acknowledged for the financial support. Authors thank Dr. Nail Yıldırım (General Directorate of Mineral Research and Exploration, MTA) for his help during field studies and Prof. Jens C.Ø. Andersen (University of Exeter) for his assistance during EPMA analysis of sulfides. The authors are grateful to all anonymous referees for their critical comments that improved the manuscript. Astrid Holzheid (Editor-in-Chief) is acknowledged for editorial handling and comments.

Appendix A. Supplementary data

Supplementary data to this article can be found online at https://doi.org/10.1016/j.chemer.2025.126326.

References

Akgül, B., 2015. Geochemical associations between fluorite mineralization and A-type shoshonitic magmatism in the Keban Elazig area, East Anatolia, Turkey. J. Afr. Earth Sci. 111, 222–230.

Akıska, S., 2020. Crystallization conditions and compositional variations of silicate and sulfide minerals in the Pb-Zn skarn deposits, Biga peninsula, NW Turkey. Ore Geol. Rev. 118, 103322.

Akıska, S., Demirela, G., Sayılı, S.I., 2013. Geology, mineralogy and the Pb, S isotope study of the Kalkim Pb-Zn ± cu deposits, Biga peninsula, NW Turkey. J. Geosci. 58, 379–396.

Anderson, G.M., 1973. The hydrothermal transport and deposition of galena and sphalerite near 100°C. Econ. Geol. 68, 80–492. https://doi.org/10.2113/gsecongeo.68.4.480.

Asutay, H.J., 1988. The geology of Baskil (Elazığ) vicinity and petrology of Baskil magmatics. Bull. Miner. Res. Explor. 107, 46–72.

Ault, K.M., Williams-Jones, A.E., 2004. Sulfur and lead isotope study of the El Mochıto Zn-Pb-ag deposit. Econ. Geol. 1223–1231.

Baker, T., Lang, J.R., 2003. Reconciling fluid inclusion types, fluid processes and fluid sources in skarns: an example from the Bismark deposit, Mexico. Mineral. Deposita 38, 474–495.

Baker, T., Van Achterberg, E., Ryan, C.G., Lang, J.R., 2004. Composition and evolution of ore fluids in a magmatic-hydrothermal skarn deposit. Geology 32, 117–120. https://doi.org/10.1130/G19950.1.

Balçık, A., Tüfekçi, M.Ş., Koyuncu, M., Ulutürk, Y., 1978. Keban madeni Derebaca ve Fırat Ocağı geliştirme raporu. MTA Derleme No: 6452.

Barnes, H.L., 1979. Geochemistry of Hydrothermal Ore Deposits, 2nd edn. Wiley, New York.

Barnes, H.L., 1997. Geochemistry of Hydrothermal Ore Deposits, 3rd edn. Wiley, New York.

Barton, P.B., Bethke, P.M., 1987. Chalcopyrite disease in sphalerite: pathology and epidemiology. Am. Mineral. 72, 451–467.

Barton, P.B., Toulmin, P., 1966. Phase relations involving sphalerite in the Fe-Zn-S system. Econ. Geol. 61, 815–849.

Bauer, M.E., Burisch, M., Ostendorf, J., Krause, J., Frenzel, M., Seifert, T., Gutzmer, J., 2019a. Trace element geochemistry of sphalerite in contrasting hydrothermal fluid systems of the Freiberg district, Germany: Insights from LA-ICP-MS analysis, near-infrared light microthermometry of sphalerite-hosted fluid inclusions, and sülfür isotope geochemistry. Mineral. Deposita 54 (2), 237–262.

Bauer, M.E., Seifert, T., Burisch, M., Krause, J., Richter, N., Gutzmer, J., 2019b. Indium bearing sulfides from the Hämmerlein skarn deposit, Erzgebirge, Germany: evidence for late-stage diffusion of indium into sphalerite. Mineral. Deposita 54, 175–192.

Bodnar, R.J., 1995. Fluid-inclusion evidence for a magmatic source for metals in porphyry copper deposits. In: Thompson, J.F.H. (Ed.), Magmas, Fluids, and Ore Deposits, Mineralogical Association of Canada Short Course Series, 23, pp. 139–152.

Bodnar, R.J., 2003. Introduction to aqueous fluid systems. In: Mineralogical Association of Canada Short Course Series, 32, pp. 81–99.

Bodnar, R.J., Vityk, M.O., 1994. Interpretation of microthermometric data for H2O-NaCl fluid inclusions. In: Vivo, B.D., Frezotti, M.L. (Eds.), Fluid Inclusions in Mineral, Methods, and Applications. Virginia Tech, Blacksburg, VA, pp. 117–130.

Bodnar, R.J., Burnham, C.W., Sterner, S.M., 1985. Synthetic fluid inclusions in natural quartz. III. Determination of phase equilibrium properties in the system H_2O–NaCl to 1000 °C and 1500 bars. Geochim. Cosmochim. Acta 49 (9), 1861–1873.

Bodnar, R.J., Lecumberri-Sanchez, P., Moncada, D., Steele-MacInnis, M., 2014. Fluid inclusions in hydrothermal ore deposits. In: Holland, H.D., Turekian, K.K. (Eds.), Treatise on Geochemistry, second ed. Elsevier, Oxford, pp. 119–142.

Bouzari, F., Clark, A.H., 2006. Prograde evolution and geothermal affinities of a major porphyry copper deposit: the Cerro Colorado hypogene protore, I Regin, northern Chile. Econ. Geol. 101, 95–134.

Bowman, J.R., 1998. Stable-isotope systematics of skarns. In: Mineral. Association of Canada Short Course Series, 26, pp. 99–145.

Bowman, J.R., O'Neil, J.R., Essene, J.R., 1985. Contact skarn formation et Elkhorn, Montana, II: origin and evolution of C-O-H skarn fluids. Am. J. Sci. 285, 621–660.

Boztuğ, D., Harlavan, Y., Arehart, G.B., Satır, M., Avcı, N., 2007. K-Ar age, whole-rock and isotope geochemistry of A-type granitoids in the Divriği-Sivas region, eastern-Central Anatolia, Turkey. Lithos 97, 193–218.

Brown, P.E., Hagemann, S.G., 1995. MacFlincor and its application to fluids in Archean lode-gold deposits. Geochim. Cosmochim. Acta 59 (19), 3943–3952.

Brueckner, S.M., Piercey, S.J., Pilote, J.C., Layne, G.D., Sylvester, P.J., 2016. Mineralogy and mineral chemistry of the metamorphosed and precious metal-bearing Ming deposit, Canada. Ore Geol. Rev. 72, 914–939.

Burnham, C.W., Ohmoto, H., 1980. Late-stage processes of felsic magmatism. Mining Geology Special Issue 8, 1–11.

Burt, D.M., 1977. Mineralogy and petrology of skarn deposits. Rend. Soc. Ital. Mineral. Petrol. 33 (2), 859–873.

Çalık, A., Öngen, S., 2000. Keban skarn oluşumu, KD Elazığ bölgesi. İstanbul Üniversitesi Mühendislik Fakültesi Yerbilimleri Dergisi 13, 1–2.

Candela, P.A., Holland, H.D., 1986. A mass transfer model for copper and molybdenum in magmatic hydrotheral systems: the origin of porphyry-type ore deposits. Econ. Geol. 81, 1–19.

Candela, P.A., Piccoli, P.M., 2005. Magmatic processes in the development of porphyry-type ore systems. Econ. Geol. 25–37, 100th Anniversary.

Çelebi, H., 1997. Geochemistry of silverbearing manganese ores of West–Euphrates sector of lead - silver deposit Keban (Elazığ). Geological Bulletin of Turkey 40 (1), 19–36.

Çelebi, H., Hanelçi, S., 1998. Geochemical and geostatistical studies on Mn-Fe ores of the deposit Keban district, Elazig/Turkey province. Geol. Yearb. D 108, 3–33.

Chelle-Michou, C., Chiaradia, M., 2017. Amphibole and apatite insights into the evolution and mass balance of cl and s in magmas associated with porphyry copper deposits. Contrib. Mineral. Petrol. 172, 105. https://doi.org/10.1007/s00410-017-1417-2.

Chen, F.C., Deng, J., Shu, Q.H., Li, G.J., Cui, X.L., Zhao, F., Wang, Q.F., 2017. Geology, fluid inclusion and stable isotopes (O, S) of the Hetaoping distal skarn Zn-Pb deposit, northern Baoshan block, SW China. Ore Geol. Rev. 90, 913–927.

Clark, I.D., Fritz, P., 1997. Environmental Isotopes in Hydrogeology. Lewis Publishers, CRC Press, New York, p. 352.

Cook, N.J., Ciobanu, C.L., Pring, A., Skinner, W., Danyushevsky, L., Shimizu, M., Saini-Eidukat, B., Melcher, F., 2009. Trace and minor elements in sphalerite: a LA-ICP-MS study. Geochim. Cosmochim. Acta 73, 4761–4791.

Dai, J., Xue, C., Chi, G., Ji, H., Zhao, X., Zhao, Y., Symons, D.T.A., 2019. Geological, geochronological and geochemical characteristics and genesis of the Arqiale skarn Zn-Pb deposit, Western Tianshan, Northwest China. Ore Geol. Rev. 106, 79–96.

Demir, Y., Dişli, A., 2020. Fluid inclusion and stable isotope constraints (C, O, H) on the DağbaşıFe–Cu–Zn skarn mineralization (Trabzon, NE Turkey). Ore Geol. Rev. 116, 103235.

Dewey, J.F., Hempton, M.R., Kıdd, W.S.F., Şaroğlu, F., Şengör, A.M.C., 1986. Shortening of continental lithosphere: the neotectonics of eastern Anatolia – a young collision zone. In: Coward, M.P., Ries, A.C. (Eds.), Collisional Tectonics. Geological Society of London Special Publications, 19, 3–36.

Ding, Q., Yan, W., Zhang, B., 2016. Sulfur- and lead-isotope geochemistry of the Balugou cu-Pb-Zn skarn deposit in the Wulonggou area in the eastern Kunlun Orogen, NW China. J. Earth Sci. 27 (5), 740–750.

Ding, T., Tan, T., Wang, J., Ma, D., Lu, J., Zhang, R., Liang, J., Wu, B., 2022. Multiple sources for the Baoshan polymetallic cu–Mo–Pb–Zn deposit, southern Hunan Province, China: insights from in situ LA–MC–ICP–MS sulfur isotopic compositions. Ore Geol. Rev. 143, 104808.

Driesner, T., Heinrich, C.A., 2007. The system H2O-NaCl. Part I. Correlation formulae for phase relations in temperature-pressure-composition space from 0 to 1000 °C, 0 to 5000 bar, and 0 to 1 XNaCl. Geochim. Cosmochim. Acta 71, 4880–4901.

Drummond, S.E., Ohmoto, H., 1985. Chemical evolution and mineral deposition in boiling hydrothermal systems. Econ. Geol. 80, 126–147.

Einaudi, M.T., Burt, D.M., 1982. Introduction: terminology, classification, and composition of skarn deposits. Econ. Geol. 77, 745–754.

Einaudi, M.T., Meinert, L.D., Newberry, R.J., 1981. Skarn deposits. Econ. Geol. 317–391, 75th Anniversary.

Ersoy, Y.E., Uysal, İ., Candan, O., Palmer, M.R., Müller, D., 2024. Petrogenesis of late Campanian alkaline igneous rocks in eastern Anatolia: magmatism related to a subduction transform edge propagator (STEP) fault? Int. Geol. Rev. 66 (2), 533–555.

Ertürk, M.A., Sar, A., Rizeli, M.E., 2022. Petrology, zircon U–Pb geochronology and tectonic implications of the A1-type intrusions: Keban region, eastern Turkey. Geochemistry 82, 125882.

Fournier, R.O., 1987. Conceptual models of brine evolution in magmatic–hydrothermal systems. In: Decker, R.W., Wright, T.L., Stauffer, P.H. (Eds.), Volcanism in Hawaii, 1350. Geological Survey Professional Paper, pp. 1487–1506.

Frank, M.R., Candela, P.A., Piccoli, P.M., 2003. Alkali exchange equilibria between a silicate melt and coexisting magmatic volatile phase: an experimental study at 800 °C and 100 MPa. Geochim. Cosmochim. Acta 67 (7), 1415–1427. https://doi.org/10.1016/S0016-7037(02)01181-X.

Frenzel, M., Hirsch, T., Gutzmer, J., 2016. Gallium, germanium, indium, and other trace and minor elements in sphalerite as a function of deposit type—a meta-analysis. Ore Geol. Rev. 76, 52–78.

Frenzel, M., Voudouris, P., Cook, N.J., Ciobanu, C.L., Gilbert, S., Wade, B.P., 2021. Evolution of a hydrothermal ore-forming system recorded by sulfide mineral chemistry: a case study from the Plaka Pb-Zn-ag deposit, Lavrion, Greece. Mineral. Deposita 57, 417–438. https://doi.org/10.1007/s00126-021-01067-y.

Gao, W., Ye, L., Cheng, Z.T., Yang, Y.L., 2011. Characteristics of isotope geochemistry of Hetaoping Pb-Zn ore in Baoshan, Yunnan Province, China. Acta Mineral. Sin. 31, 578–586 in Chinese with English abstract.

Gaspar, M., Knaack, C., Meinert, L.D., Moretti, R., 2008. REE in skarn systems: a LA-ICPMS study of garnets from the crown Jewel gold deposit. Geochim. Cosmochim. Acta 72, 185–205. https://doi.org/10.1016/j.gca.2007.09.033.

George, L.L., Cook, N.J., Ciobanu, C.L., 2016. Partitioning of trace elements in cocrystallized sphalerite–galena–chalcopyrite hydrothermal ores. Ore Geol. Rev. 77, 97–116.

Ghosh, U., Upadhyay, D., 2022. The retrograde evolution of F-rich skarns: clues from major and trace element chemistry of garnet, scheelite, and vesuvianite from the Belka Pahar wollastonite deposit, India. Lithos 422-423, 106750.

Göncüoğlu, M.C., 2011. Kütahya Bolkardağ Kuşağının Jeolojisi. MTA Derg. 142, 227–282.

Govindarao, B., Pruseth, K.L., Mishra, B., 2018. Sulfide partial melting and chalcopyrite disease: an experimental study. J. Bone Miner. Res. 103, 1200–1207.

Groat, L.A., Hawthorne, F.C., Ercit, T.S., 1992. The chemistry of vesuvianite. Can. Mineral. 30 (1), 19–48.

Halden, N.M., 1996. Determination of lyapounov exponents to characterize the oscillatory distribution of trace elements in minerals. Can. Mineral. 34, 1127–1135.

Halter, W.E., Heinrich, C.A., Pettke, T., 2005. Magma evolution and the formation of porphyry cu-au ore fluids: evidence from silicate and sulfide melt inclusions. Mineral. Deposita 39 (8), 845–863. https://doi.org/10.1007/s00126-004-0457-5.

Hanelçi, Ş., 1989. Keban (Elazığ) civarı eski imalat pasalarının Au ve Ag açısından önemi. report to Etibank, 48 pp., Keban. (Unpublished)..

Hanelçi, Ş., 1991. Zeryan Dere-Siftil Tepe (Keban-Elazığ) metalojenezinin incelenmesi. Doktora Tezi, İstanbul Üniversitesi Fen Bilimleri Enstitüsü..
He, W., Yang, L., Brugger, J., McCuaig, T.C., Lu, Y., Bao, X., Xing, Y., 2017. Hydrothermal evolution and ore genesis of the Beiya giant Au polymetallic deposit, western Yunnan, China: Evidence from fluid inclusions and H–O–S–Pb isotopes. Ore Geol. Rev. 90, 847–862.
Heinrich, C.A., 2007. Fluid-fluid interactions in magmatic-hydrothermal ore formation. Rev. Mineral. Geochem. 65, 363–387.
Hoefs, J., 1987. Stable Isotope Geochemistry. Springer Verlag, Berlin.
Hoefs, J., 2009. Stable Isotope Geochemistry, 6th edn. Springer, Berlin, Heidelberg, p. 285.
Holloway, J.R., 1976. Fluids in the evolution of granitic magmas: consequences of finite CO2 solubility. Geol. Soc. Am. Bull. 87, 1513–1518.
Holness, M.B., 1997. Fluid flow paths and mechanism of fluid infiltration in carbonates during contact metamorphism: the Beinn a Dubhaich aureole, Skye. J. Metamorph. Geol. 15, 59–70.
Hou, Z.Q., Duan, L., Lu, Y., Zheng, Y., Zhu, D., Yang, Z., 2015. Lithospheric architecture of the Lhasa terrane and its control on ore deposits in the Himalayan-Tibetan orogen. Econ. Geol. 110, 1541–1575.
Hu, Y., Wei, C., Ye, L., Huang, Z., Danyushevsky, L., Wang, H., 2021. LA-ICP-MS sphalerite and galena trace element chemistry and mineralization-style fingerprinting for carbonate-hosted Pb-Zn deposits: perspective from early Devonian Huodehong deposit in Yunnan, South China. Ore Geol. Rev. 136, 104–253.
Huang, H., 2014. The Research on Geological Characteristics and Metallogenesis of the Jinchanghe Fe-cu-Pb-Zn Polymetallic Deposit, Yunnan Province (M.Sc. Thesis). China University of Geosciences (Beijing), pp. 1–82 in Chinese with English abstract.
İmer, A., Richards, J.P., Creaser, R.A., 2013. Age and tectonomagmatic setting of the Çöpler-Kabataş magmatic complex and porphyry-epithermal au deposit, east Central Anatolia, Turkey. Mineral. Deposita 48, 557–583.
İmer, A., Richards, J.P., Creaser, R.A., Spell, T.L., 2015. The late Oligocene Cevizlidere cu-au-Mo deposit, Tunceli Province, eastern Turkey. Mineral. Deposita 50, 245–263.
İmer, A., Richards, J.P., Muehlenbachs, K., 2016. Hydrothermal evolution of the Çöpler porphyry-epithermal au deposit, Erzincan Province, central eastern Turkey. Econ. Geol. 111, 1619–1658.
Jiang, Z., Zhang, Z., Duan, S., Lv, C., Dai, Z., 2021. Genesis of the sediment-hosted Haerdaban Zn-Pb deposit, Western Tianshan, NW China: constraints from textural, compositional and sulfur isotope variations of sulfides. Ore Geol. Rev. 139, 104527.
Kalendar, L., Hanelçi, S., 2004. General features of copper mineralization in the eastern Euphrates, Keban-Elazığ area, Turkey. J. Geol. Soc. India 64, 655–665.
Kalender, L., 2000. Geology, Origin and Economic Importance of the Copper Mineralization of Keban (Elazig), East Euphrates Kebandere Area, Ph.D. Thesis, Firat University, Elazığ, Turkey, pp.100 (in Turkish)..
Kalender, L., 2011. Oxygen, carbon, and sulfur isotope studies in the Keban Pb-Zn deposits, eastern Turkey: an approach on the origin of hydrothermal fluids. J. Afr. Earth Sci. 59 (4–5), 341–348.
Kaya, A., 2016. Tectono-stratigraphic reconstruction of the Keban metamorphites based on new fossil findings, eastern Turkey. J. Afr. Earth Sci. 124, 245–257.
Kaymakçı, N., Inceöz, M., Ertepınar, P., 2006. 3D architecture and Neogene evolution of the Malatya Basin: inferences for the kinematics of the Malatya and Ovacik fault zones. Turk. J. Earth Sci. 15, 123–154.
Kelley, K.D., Leach, D.L., Johnson, C.A., Clark, J.L., Fayek, M., Slack, J.F., Anderson, V. M., Ayuso, R.A., Ridley, W.I., 2004. Textural, compositional, and sulfur isotope variations of sulfide minerals in the red dog Zn-Pb-ag deposits, Brooks Range, Alaska: implications for ore formation. Econ. Geol. 99 (7), 1509–1532.
Kırat, E., 2020. Mineralogical, Geochemical and Isotopic Characteristics of the Keban Skarn Deposit (Elazığ-East Anatolia). Ph.D. Thesis, Ankara University, Graduate School of Natural and Applied Sciences (in Turkish), pp. 207.
Kürüm, S., 2013. Geochemical and Sr Nd isotopic significance of post-collisional Keban a type syenites, Elazığ, southeastern Turkey. Carpathian J. Earth Environ. Sci. 8 (4), 209–220.
Kürüm, S., Önal, A., Boztuğ, D., Spell, T., Arslan, M., 2008. 40Ar/39Ar age and geochemistry of the post-collisionalMiocene Yamadağ volcanics in the Arapkir area (Malatya Province), eastern Anatolia, Turkey. J. Asian Earth Sci. 33, 229–251.
Kuşcu, İ., 2019. Skarns in Turkey. In: Pirajno, F., Ünlü, T., Dönmez, C., Şahin, M.B. (Eds.), modern approaches in solid earth sciences, Mineral Resources of Turkey 16, pp. 307–331.
Kuşcu, İ., Yilmazer, E., Demirela, G., 2002. A new Fe-oxide-cu-au (Olympic dam type) perspective to skarn type iron oxide mineralization in Sivas-Divriği region. Geological Bulletin of Turkey 45 (2).
Kuşcu, İ., Gençalioğlu-Kuşcu, G., Tosdal, R.M., Ullrich, T., Friedman, R., 2010. Magmatism in the southeastern Anatolian orogenic belt: transition from arc to postcollisional setting in an evolving orogen. Geol. Soc. Lond. Spec. Publ. 340, 437–460.
Kuşcu, İ., Yılmazer, E., Bayır, S., Sezerer-Kuru, G., Güleç, N., Demirela, G., Gençalioğlu-Kuşcu, G., Kaymakçı, N., 2011. U-Pb and Ar-Ar age dating and fluid inclusion constraints on the genesis of Hasançelebi Iron oxide-copper-(gold) mineralization, Malatya (Turkey). Econ. Geol. 106, 261–288.
Kuşcu, I., Tosdal, R.M., Gencalioğlu-Kuşcu, G., Friedman, R., Ullrich, T.D., 2013. Late cretaceous to middle Eocene magmatism and metallogeny of a portion of the southeastern Anatolian orogenic belt, east-Central Turkey. Econ. Geol. 108 (4), 641–666.
Kuşcu, I., Tosdal, R.M., Gencalioğlu-Kuşcu, G., 2019. Episodic porphyry cu (-Mo-au) formation and associated magmatic evolution in Turkish Tethyan collage. Ore Geol. Rev. 107, 119–154.
Kwak, T.A.P., 1986. Fluid inclusions in skarns (carbonate replacement deposits). J. Metamorph. Geol. 4, 363–384.
Kwak, T.A.P., Tan, H., 1981. The importance of CaCl2 in fluid composition trends; evidence from the King Island (dolphin) skarn deposit. Econ. Geol. 76 (4), 955–960.
Large, R.R., 1992. Australian volcanic-hosted massive sulfide deposits: features, styles, and genetic models. Econ. Geol. 87, 471–510.
Lecumberri-Sanchez, P., Luo, M., Steele-MacInnis, M., Runyon, S.E., Sublett Jr., D.M., Klyukin, Y.I., Bodnar, R.J., 2020. Synthetic fluid inclusions XXII: properties of H_2O-NaCl ± KCl fluid inclusions trapped under vapor- and salt-saturated conditions with emphasis on the effect of KCl on phase equilibria. Geochim. Cosmochim. Acta 272, 78–92.
Lessing, P., Standish, R.P., 1973. Zoned garnet from crested Butte. Colorado. American Mineralogist 58 (9–10), 840–842.
Li, M., Zheng, Y., Feng, Q., Xu, J., Wu, S., Sun, G., 2020. Ore genesis of skarn mineralization in continental collision orogens: a case study from the Pusangguo co-bearing cu–Pb–Zn deposit in Tibet. Ore Geol. Rev. 122, 103523.
Liu, L., Zhou, T., Zhang, D., Liu, G., Zhao, Z., Sun, J., White, N.C., 2021. Major and trace elements analyses of garnet from the Haobugao Zn-Fe-Sn polymetallic deposit, Northeast China: implications for skarn formation and hydrothermal fluid evolution. Ore Geol. Rev. 138, 104337. https://doi.org/10.1016/j.oregeorev.2021.104337.
Liu, Z., Zhu, D.-C., Rezeau, H., Jagoutz, O., Wang, Q., Eyüboğlu, Y., 2022. Late cretaceous transition from calc-alkaline to alkaline magmatism in the eastern Anatolian plateau: implications for microblock collision timing. J. Petrol. 63, 1–24.
Lockington, J.A., Cook, N.J., Ciobanu, C.L., 2014. Trace and minor elements in sphalerite from metamorphosed sulphide deposits. Mineral. Petrol. 108 (6), 873–890.
Lueth, V.W., Megaw, P.K.M., Pingitore, N.E., Goodell, P.C., 2000. Systematic variation in galena solid-solution compositions at Santa Eulalia, Chihuahua. Mexico. Econ. Geol. 95 (8), 1673–1687.
Megaw, P.K.M., 1998. Carbonate-hosted Pb-Zn-ag-cu-au replacement deposits: an exploration perspective. In: Mineralogical Association of Canada Short Course Series, 26, pp. 337–357.
Megaw, P.K.M., Ruiz, J., Titley, S.R., 1988. High-temperature, carbonate-hosted ag-Pb-Zn(cu) deposits of northern Mexico. Econ. Geol. 83, 1856–1885.
Meinert, L.D., 1983. Variability of skarn deposits—Guides to exploration. In: Boardman, S.J. (Ed.), Revolution in the Earth Sciences. Kendall-Hunt, Dubuque, Iowa, pp. 301–316.
Meinert, L.D., 1987. Skarn zonation and fluid evolution in the groundhog mine, central Mining District, New Mexico. Econ. Geol. 82, 523–545.
Meinert, L.D., 1992. Skarns and skarn deposits. Geosci. Can. 19, 145–162.
Meinert, L.D., 1997. Application of skarn deposit zonation models to mineral exploration. Explor. Min. Geol. 6, 185–208.
Meinert, L.D., Hefton, K.K., Mayes, D., Tasiran, I., 1997. Geology, zonation, and fluid evolution of the big gossan Cu-Au skarn deposit, Ertsberg district. Irian Jaya. Econ. Geol. 92 (5), 509–534.
Meinert, L.D., Hedenquist, J.W., Satoh, H., Matsuhisa, Y., 2003. Formation of anhydrous and hydrous skarn in cu-au ore deposits by magmatic fluids. Econ. Geol. 98 (1), 147–156.
Meinert, L.D., Diple, G.M., Nicolescu, S., 2005. World skarn deposits, Society of Economic Geologist, Inc. Economic Geology 100th Anniversary Volume 299–336.
Misra, K.C., 2000. Understanding Mineral Deposits. Kluwer Academic Publications, Dordrecht, pp. 414–449.
Moix, P., Beccaletto, L., Kozur, H.W., Hochard, C., Rosselet, F., Stampfli, G.M., 2007. A new classification of the Turkish terranes and sutures and its implication for the paleotectonic history of the region. Tectonophysics 451, 7–39.
MTA, 1989. Fluorite deposits of Turkey. Publ. of Mineral Research and Exploration Gen. Dir., Ankara, No, p. 179.
Nabatian, G., Li, X.-H., Honarmand, M., Melgarejo, J.C., 2017. Geology, mineralogy and evolution of iron skarn deposits in the Zanjan district, NW Iran: constraints from U-Pb dating, Hf and O isotope analyses of zircons and stable isotope geochemistry. Ore Geol. Rev. 84, 42–66.
Nagase, T., Kojima, S., 1997. An SEM examination of the chalcopyrite disease texture and its genetic implications. Mineral. Mag. 61, 89–97.
Nakano, T., 1998. In: Lentz, D.R. (Ed.), Pyroxene Geochemistry as an Indicator for Skarn Metallogenesis in Japan, Mineralized Intrusion-Related Skarn Systems, Mineralogical Association of Canada Short Course Series, 26, pp. 147–167.
Nakano, T., Yoshino, T., Shimazaki, H., Shimizu, M., 1994. Pyroxene composition as an Indicator in the classification of skarn deposits. Econ. Geol. 89, 1567–1580.
Newberry, R.J., 1987. Use of intrusive and calc-silicate compositional data to distinguish contrasting skarn types in the Darwin polymetallic skarn district, California, USA. Mineral. Deposita 22, 207–215.
Newberry, R.J., Swanson, S.E., 1986. Scheelite skarn granitoids: an evaluation of the roles of magmatic source and process. Ore Geol. Rev. 1, 57–81.
Nurlu, N., Köksal, S., Kohút, M., 2022. Late Cretaceous volcanic arc magmatism in southeast Anatolian orogenic belt: constraints from whole-rock, mineral chemistry, Sr–Nd isotopes and U–Pb zircon ages of the Baskil Intrusive Complex (Malatya, Turkey). Geol. J. 57, 3048–3073.
Ohmoto, H., 1972. Systematics of sulfur and carbon isotopes in hydrothermal ore deposits. Econ. Geol. 67, 551–578.
Ohmoto, H., 1996. Formation of volcanogenic massive sulfide deposits: the Kuroko perspective. Ore Geol. Rev. 10, 135–177.
Ohmoto, H., Goldhaber, M.B., 1997. Sulfur and carbon isotopes. In: Barnes, H.L. (Ed.), Geochemistry of Hydrothermal Ore Deposits. J Wiley, pp. 517–611.
Ohmoto, H., Rye, R.O., 1979. Isotopes of sulfur and carbon. In: Geochemistry of Hydrothermal Ore Deposits. J Wiley, pp. 509–567.
Orhan, A., Mutlu, H., Fallick, A.E., 2011. Fluid infiltration effects on stable isotope systematics of the Susurluk skarn deposit, NW Turkey. J. Asian Earth Sci. 40, 550–568.

Özgül, N., 1976. Torosların Bazı Temel Jeoloji Özellikleri. Türkiye Jeoloji Kurultayı Bülteni 19 (1).
Öztürk, H., Altuncu, S., Hanilçi, N., Kasapci, C., Goodenough, K.M., 2019. Rare earth element-bearing fluorite deposits of Turkey: an overview. Ore Geol. Rev. 105, 423–444.
Park, C., Choi, W., Kim, H., Park, M.H., Kang, I.M., Lee, H.S., Song, Y., 2017. Oscillatory zoning in skarn garnet: implications for tungsten ore exploration. Ore Geol. Rev. 89, 1006–1018. https://doi.org/10.1016/j.oregeorev.2017.08.003.65-78.
Parlak, O., 2006. Geodynamic significance of granitoid magmatism in the southeast Anatolian orogen: geochemical and geochronogical evidence from Goksun-Afsin (Kahramanmaras, Turkey) region. Int. J. Earth Sci. 95, 609–627.
Parlak, O., Höck, V., Kozlu, H., Delaloye, M., 2004. Oceanic crust generation in an island arc tectonic setting, SE Anatolian Orogenic Belt (Turkey). Geol. Mag. 141, 583–603.
Pearce, J.A., Bender .F., J., De Long .E., S., Kidd .S.,.F., W., Low .J., P., Guner, Y., Saroglu, F., Yilmaz, Y., Moorbath, S., Mitchell .G., J., 1990. Genesis of collision volcanism in eastern Anatolia, Turkey. J. Volcanol. Geotherm. Res. 44, 189–229.
Peng, H., Zhang, C., Mao, J., Santosh, M., Zhou, Y., Hou, L., 2015. Garnets in porphyry skarn systems: a LA-ICP_MS, fluid inclusion, and stable isotope study of garnets from the Hongniu-Hongshan copper deposit, Zhongdian area, NW Yunnan province, China. J. Asian Earth Sci. 103, 229–251.
Qi, L., Liu, C., 2002. The characteristics of ore-forming fluid of dongguashan staratabound skarn cu deposit and its significance for deposit genesis. J. Changchun Univ. Sci. Technol. 32 (3), 219–224.
Ragnarsdóttir, K.V., Walther, J.V., 1985. Experimental determination of corundum solubilities in pure water between 400–700°C and 1–3 kbar. Geochim. Cosmochim. Acta 49, 2109–2115. https://doi.org/10.1016/0016-7037(85)90068-7.
Ravna, E.K., 2000. The garnet–clinopyroxene Fe^{2+}–Mg geothermometer: an updated calibration. J. Metamorph. Geol. 18, 211–219.
Raza, M.A., Shareef, M., Badireddi, V.S.S.A.N., Suryavanshi, H., Baswani, S.R., Dora, M. L., Meshram, T., Akhter, P., Raghuram, Kumarı, S, Panda, B., Saha, S.K., Maura, L.M. S., Sarkar, S.S., John, M.M., Bai, S.R.S., 2020. Multiple sulfur sources for the volcanic hosted massive sulfides in Betul Belt, Central India: evidence from the sulfide ore chemistry and sulfur isotope geochemistry. Geochemistry 80, 125632.
Ren, T., Zhang, X., Han, R., Hou, B., 2015. Carbon–oxygen isotopic covariations of calcite from Langdu skarn copper deposit, China: implications for sulfide precipitation. Chin. J. Geochem. 34 (1), 21–27.
Ren, Y., Yundeng, L., 2006. Hydrothermal colloidal pyrite in Tongling area, Anhui Province, and its metallogenic significance. Mineral Deposits 25 (S1), 95–98 in Chinese.
Richards, J.P., 2005. Cumulative factors in the generation of giant calc-alkaline porphyry cu deposits. In: Porter, T.M. (Ed.), Super Porphyry Copper and Gold Deposits: A Global Perspective, v. 1. PGC Publishing, Adelaide, pp. 7–25.
Richards, J.P., 2011. High Sr/Y arc magmas and porphyry cu ± Mo ± au deposits: just add water. Econ. Geol. 106, 1075–1081.
Rızaoğlu, T., Parlak, O., Höck, V., Koller, F., Hames, W.E., Billor, Z., 2009. Andean-type active margin formation in the eastern Taurides: geochemical and geochronological evidence from the Baskil granitoid (Elazığ, SE Turkey). Tectonophysics 473, 188–207.
Robertson, A.H.F., Parlak, O., Rızaoğlu, T., Ünlügenç, U., Inan, N., Tasli, K., Ustaömer, T., 2007. Late Cretaceous–Mid Tertiary tectonic evolution of the eastern Taurus mountains and the southern Tethyan ocean; evidence from the ElazIg region, SE Turkey. In: Ries, A.C., Butler, R.W.H., Graham, R.H. (Eds.), Deformation of the Continental Crust, Geological Society. Special Publications, London, pp. 231–270.
Roedder, E., 1979. Fluid inclusions as samples of ore fluids. In: Barnes, H.L. (Ed.), Geochemistry of Hydrothermal Ore Solutions. Wiley & Sons, Chichester.
Roedder, E., 1984. Fluid inclusions. In: Rev. Mineral, 12, pp. 12–45.
Roedder, E., Bodnar, R.J., 1980. Geological pressure determinations from fluid inclusion studies. Annu. Rev. Earth Planet. Sci. 8, 263–301.
Rollinson, H.R., 1993. Using Geochemical Data: Evaluation, Presentation, Interpretation. Longman UK.
Rye, R.O., Ohmoto, H., 1974. Sulfur and carbon isotopes and ore genesis: a review. Econ. Geol. 69, 826–842.
Rye, R.O., Hall, W.E., Ohmoto, H., 1974. Carbon, hydrogen, oxygen, and sulfur isotope study of the Darwin lead-silver-zinc deposit, Southern California. Econ. Geol. 69, 468–481.
Samson, I.M., Williams-Jones, A.E., Ault, K.M., Gagnon, J.E., Fryer, B.J., 2008. Source of fluids forming distal Zn-Pb-ag skarns: evidence from laser ablation–inductively coupled plasma–mass spectrometry analysis of fluid inclusions from El Mochito, Honduras. Geology 36, 947–950.
Savostin, L.A., Sibuet, J.C., Zonenshain, L.P., Le Pichon, X., Rolet, J., 1986. Kinematic evolution of the Tethys belt, from the Atlantic to the Pamirs since the Triassic. Tectonophysics 123, 1–35.
Scott, S.D., 1983. Chemical behaviour of sphalerite and arsenopyrite in hydrothermal and metamorphic environments. Mineral. Mag. 47, 427–435.
Seeliger, T.C., Pernicka, E., Wagner, G.A., Bwgemann, F., Strecker, S., Eibner, C., Öztunalı, Ö., Bayranlı, I., 1985. Aachaometallurgische Untersuchungen in Nord und Ostanatolien. 32. Jahrbuch des Römisch-Germanischen Zentral-Museum 597–659, Mainz.
Şengör, A.M.C., Yılmaz, Y., 1981. Tethyan evolution of Turkey: a plate tectonic approach. Tectonophysics 75, 181–241.
Shepherd, T., Rankın, A.H., Alderton, D.H.M., 1985. A Practical Guide to Fluid Inclusion Studies. Blackie-Glasgow-Lond, p. 239.
Shimazaki, H., 1976. Granitic magmas and ore deposits: 2. oxidation state of magmas and ore deposits. Mining Geol. 36, 25–35.
Shimazaki, H., 1988. Oxygen, carbon and sulfur isotope study of skarn deposits in Japan. In: Zachrisson, E. (Ed.), Proceedings of the 7th Quadrennial IAGOD Symposium. E. Schweizerbart'sche Verlagsbuchhandlung, Stuttgart, Germany, pp. 375–381.
Shimazaki, H., Shimizu, M., Nakano, T., 1986. Carbon and oxygen isotopes of calcites from Japanese skarn deposits. Geochem. J. 20, 297–310.
Shimizu, M., Shimazaki, H., 1981. Application of the sphalerite geobarometer to some skarn-type ore deposits. Mineral. Deposita 16, 45–50.
Shin, D., Lee, I., 2003. Evaluation of the volatilization and infiltration effect on the stable isotopic and mineralogical variations in the carbonate rocks adjacent to the cretaceous Muamsa granite, South Korea. J. Asian Earth Sci. 227–243.
Shinohara, H., Hedenquist, J.W., 1997. Constraints on magma degassing beneath the Far Southeast porphyry Cu-Au deposit, Philippines. J. Petrol. 38, 1741–1752.
Shu, Q., Lai, Y., Sun, Y., Wang, C., Meng, S., 2013. Ore genesis and hydrothermal evolution of the baiyinnuo'er zinc-lead skarn deposit, Northeast China: evidence from isotopes (S, Pb) and fluid inclusions. Econ. Geol. 108 (4), 835–860.
Shu, Q., Chang, Z., Mavrogenes, J., 2021. Fluid compositions reveal fluid nature, metal deposition mechanisms, and mineralization potential: an example at the Haobugao Zn-Pb skarn, China. Geology 49, 473–477.
Sillitoe, R.H., 2010. Porphyry copper systems. Econ. Geol. 105, 3–41.
Simon, A.C., Pettke, T., Candela, P.A., Piccoli, P.M., Heinrich, C.A., 2003. Experimental determination of au solubility in rhyolite melt and magnetite, constraints on magmatic au budgets. Am. Mineral. 88, 1644–1651.
Simon, A.C., Pettke, T., Candela, P.A., Piccoli, P.M., Heinrich, C.A., 2006. Copper partitioning in a melt-vapor-brine-magnetite-pyrrhotite assemblage. Geochim. Cosmochim. Acta 70 (22), 5583–5600. https://doi.org/10.1016/j.gca.2006.08.045.
Sisson, V.B., Hollister, L.S., 1990. A fluid-inclusion study of metamorphosed pelitic and carbonate rocks, south-Central Maine. Am. Mineral. 75, 59–70.
Stern, C.R., Funk, J.A., Skewes, M.A., Arevalo, A., 2007. Magmatic anhydrite in plutonic rocks at the El teniente cu-Mo deposit, Chile and the role of sulfur- and copper-rich magmas in its formation. Econ. Geol. 102 (7), 1335–1344. https://doi.org/10.2113/gsecongeo.102.7.1335.
Strmić Palinkaš, S., Palinkaš, L.A., Renac, C., Spangenberg, J.E., Lüders, V., Molnar, F., Maliqi, G., 2013. Metallogenic model of the Trepča Pb-Zn-Ag skarn deposit, Kosovo evidence from fluid inclusions, rare earth elements, and stable isotope data. Econ. Geol. 108, 135–162.
Strmić, Palinkaš S., Peltekovski, Z., Tasev, G., Serafimovski, T., Šmajgl, D., Rajič, Spangenberg, J.E., Neufeld, K., Palinkaš, L., 2018. The role of magmatic and hydrothermal fluids in the formation of the Sasa Pb-Zn-ag skarn deposit, Republic of Macedonia. Geosciences 444. https://doi.org/10.3390/geosciences8120444.
Taylor, B.E., 1986. Magmatic volatiles: isotopic variation of C, H, and S. In: Reviews in Mineralogy and Petrology, 16, pp. 185–226.
Tian, Z.-D., Leng, C.-B., Zhang, X.-C., Zafar, T., Zhang, L.-J., Hong, W., Lai, C.-K., 2019. Chemical composition, genesis and exploration implication of garnet from the Hongshan Cu-Mo skarn deposit, SW China. Ore Geol. Rev. 112, 103016. https://doi.org/10.1016/j.oregeorev.2019.103016.
Valley, J.W., 1986. Stable isotope geochemistry of metamorphic rocks. Rev. Mineral. Geochem 16, 445–490.
Van den Kerkhof, A.M., Hein, U.F., 2001. Fluid inclusion petrography. Lithos 55, 27–47.
Vázquez, R., Vennemann, T.W., Kesler, S.E., Russell, N., 1998. Carbon and oxygen isotope halos in the host limestone, El Mochito Zn-Pb-(ag) skarn massive sulfide-oxide deposit, Honduras. Econ. Geol. 93, 15–31.
Veizer, J., Holser, W.T., Wilgus, C.K., 1980. Correlation of $^{13}C/^{12}C$ and $^{34}S/^{32}S$ secular variations. Geochim. Cosmochim. Acta 44, 579–587.
Walther, J.V., 1997. Experimental determination and interpretation of the solubility of corundum in H_2O between 350 and 600°C from 0.5 to 2.2 kbar. Geochim. Cosmochim. Acta 61, 4955–4964. https://doi.org/10.1016/S0016-7037(97)00282-2.
Wang, P., Dong, G.C., Li, X.F., Chen, W., Li, J.X., Tao, X.X., 2017. Metallogenic sources of the Hongshan-Hongniu copper deposit in northwestern Yunnan: constraints from mineralogy and stable isotope. Geosci. Front. 24, 176–193 in Chinese with English abstract.
Wang, X., Wang, S., Zhang, H., Wang, Y., Zhu, X., Yang, X., 2023. Geochemical characteristics of the mineral assemblages from the Niukutou Pb-Zn skarn deposit, East Kunlun Mountains, and their metallogenic ımplications. Minerals 13 (18).
Wilkinson, J.J., 2001. Fluid inclusions in hydrothermal ore deposits. Lithos 55, 229–272.
Williams-Jones, A.E., Heinrich, C.A., 2005. 100th anniversary special paper: vapor transport of metals and the formation of magmatic-hydrothermal ore deposits. Econ. Geol. 100 (7), 1287–1312. https://doi.org/10.2113/gsecongeo.100.7.1287.
Williams-Jones, A.E., Samson, I.M., Ault, K.M., Gagnon, J.E., Fryer, B.J., 2010. The genesis of distal zinc skarns: evidence from the Mochito deposit, Honduras. Econ. Geol. 105, 1411–1440.
Wright, K., Gale, J.D., 2010. A first principles study of the distribution of iron in sphalerite. Geochim. Cosmochim. Acta 74, 3514–3520.
Xing, B., Mao, J., Xiao, X., Liu, H., Jia, F., Wang, S., Huang, W., Li, H., 2021. Genetic discrimination of the Dingjiashan Pb-Zn deposit, SE China, based on sphalerite chemistry. Ore Geol. Rev. 135, 104212.
Xu, J., Ciobanu, C.L., Cook, N.J., Zheng, Y., Sun, X., Wade, B.P., 2016. Skarn formation and trace elements in garnet and associated minerals from Zhibula copper deposit, Gangdese belt, southern Tibet. Lithos 262, 213–231.
Xu, R., Li, W.-C., Deng, M.-G., Zhou, J.-X., Ren, T., Yu, H.-J., 2019. Genesis of the superlarge Luziyuan Zn-Pb-Fe (-cu) distal skarn deposit in western Yunnan (SW China): insights from ore geology and C-H-O-S isotopes. Ore Geol. Rev. 107-944-959. https://doi.org/10.1016/j.oregeorev.2019.03.015.
Xue, C.D., Han, R.S., Yang, H.L., Yang, Z.M., Tian, S.H., Liu, Y.Q., Hao, B.W., 2008. Isotope geochemical evidence for ore-forming fluid resources in Hetaoping Pb-Zn

deposit, Baoshan, northwestern Yunnan. Mineral. Deposita 27, 243–252 in Chinese with English abstract.
Yang, Y.L., Ye, L., Cheng, Z.T., Bao, T., 2013. Origin of fluids in the Hetaoping Pb–Zn deposit, Baoshan–Narong–Dongzhi block metallogenic belt, Yunnan Province, SW China. J. Asian Earth Sci. 73, 362–371.
Yazgan, E., 1984. Geodynamics Evolution of the Eastern Taurus Region. In: Tekeli, O., Göncüoğlu, M.C. (Eds.), Geology of the Taurus Belt. International Symposium Proceedings, pp. 199–208.
Ye, L., Cook, N.J., Ciobanu, C.L., Yuping, L., Qian, Z., Tiegeng, L., Wei, G., Yulong, Y., Danyushevskiy, L., 2011. Trace and minor elements in sphalerite from base metal deposits in South China: a LA-ICPMS study. Ore Geol. Rev. 39 (4), 188–217.
Yiğit, Ö., 2009. Mineral deposits of Turkey in relation to Tethyan Metallogeny: implications for future mineral exploration. Econ. Geol. 104 (1), 19–51.
Yıldırım, E., Yıldırım, N., Dönmez, C., Koh, S.-M., Günay, K., 2019b. Mineralogy, rare earth elements geochemistry and genesis of the Keban-West Euphrates (cu-Mo)-Pb-Zn skarn deposit (eastern Taurus metallogenic belt, E Turkey). Ore Geol. Rev. 114, 103102.
Yıldırım, N., Eroğlu, M., Çetiner, L., 2019a. Elazığ-Keban-Pınarlar köyü yöresindeki ar: 201300540 no'lu (er: 3305655) IV. grup ruhsat sahasına ait (Cu-Mo-Fe-Zn-Pb-Ag-Au ve Jips) madenlerin buluculuk talebine esas kaynak tahmin raporu Cilt-I. MTA Raporu.
Yılmaz, A., Ünlü, T., Sayılı, S., 1992. Keban (Elazığ) kurşun-çinko cevherleşmelerinin kökenine bir yaklaşım: ön çalışma. MTA Dergisi 114, 47–70.
Zajacz, Z., Halter, W., 2009. Copper transport by high temperature, sulfur-rich magmatic vapor: evidence from silicate melt and vapor inclusions in a basaltic andesite from the Villarrica volcano (Chile). Earth Planet. Sci. Lett. 282 (1–4), 115–121. https://doi.org/10.1016/j.epsl.2009.03.006.
Zheng, Y.C., Fu, Q., Hou, Z.Q., Yang, Z.S., Huang, K.X., 2015. Metallogeny of the northeastern Gangdese Pb-Zn-Fe-Mo-W polymetallic belt in the Lhasa terrane, southern Tibet. Ore Geol. Rev. 70, 510–532.
Zheng, Y.F., 2001. Theoretical modeling of stable isotope systems and its applications to geochemistry of hydrothermal ore deposits. Mineral. Deposita 20, 56–71.
Zhong, S., Fen, C., Seltmann, R., Dolgopolova, A., Andersen, J.C.Ø., Li, D., Yu, M., 2018. Sources of fluids and metals and evolution models of skarn deposits in the Qimantagh metallogenic belt: a case study from the Weibao deposit, East Kunlun Mountains, northern Tibetan plateau. Ore Geol. Rev. 93, 19–37.
Zhuang, L., Song, Y., Liu, Y., Fard, M., Hou, Z., 2019. Major and trace elements and sülfür isotopes in two stages of sphalerite from the world-class Angouran Zn–Pb deposit, Iran: implications for mineralization conditions and type. Ore Geol. Rev. 109, 184–200.